

## Application of advanced synthesis and sintering technologies in the preparation of high-entropy ceramics: A review

Jiahang Liu<sup>a</sup>, Zhe Lu<sup>a,\*</sup>, Yeon-Gil Jung<sup>b,\*</sup>, Jeong-Hun Son<sup>b</sup>, Guanlin Lyu<sup>c</sup>, YiYong Wang<sup>a</sup>, Jing Zhang<sup>d</sup>, Yanwen Zhou<sup>a</sup> and Yan Li<sup>a</sup>

<sup>a</sup>School of Materials and Metallurgical Engineering, University of Science and Technology Liaoning, Anshan 114051, China

<sup>b</sup>Department of Materials Convergence and System Engineering, Changwon National University, Changwon 51140, Korea

<sup>c</sup>Key Lab of New Ceramics and Fine Processing, School of Materials Science and Engineering, Tsinghua University, Beijing 100084, China

<sup>d</sup>Department of Mechanical Engineering, Indiana University-Purdue University Indianapolis, Indianapolis, IN 6202, USA

The high-entropy ceramic is a new type of ceramic material system that has been gradually developed based on high-entropy alloy in recent years, and its emergence provides new design concepts and technical routes for the development of non-metallic materials with excellent performance. Due to the complex elemental composition and unique high-entropy effect of high-entropy ceramic, the use of conventional solid-state synthesis and solid-state sintering techniques requires long holding times and high temperatures. With the development of advanced synthesis and sintering technologies, some researchers have adopted novel methods to prepare high-entropy ceramics, and have achieved excellent results in shortening the cycle time of powder synthesis, lowering the sintering temperature, and optimizing the properties of ceramics. This work analyzed and summarized the research on advanced synthesis and sintering techniques for the preparation of high-entropy ceramics, discussed the principles, characteristics, advantages, and development prospects of different synthesis techniques as well as sintering techniques, and looked forward to the future direction of research on the synthesis and sintering methods of high-entropy ceramics.

**Keywords:** High-entropy ceramics, Synthesis, Sintering, Thermophysical properties, Review.

### Introduction

Human society's progress and development have placed increasing demands on material properties, which motivates researchers to explore new material design concepts and develop novel material systems. In recent years, new materials with excellent performance have emerged and become research hotspots one after another [1]. A high-entropy material is a new type of multicomponent material composed of multiple elements in equal or nearly equal molar ratios [2]. The concept of high-entropy was first introduced in the late 1990s and applied to high-entropy alloys by Ye et al. [3, 4]. High-entropy materials break the traditional concept of material design and exhibit many structural and physical properties that are different from those of traditional materials, including excellent fracture resistance, tensile strength, corrosion resistance, and oxidation resistance [5-8]. At the beginning of the 21st century, Centor et al. [9] proposed the concept of multi-major element alloys, and then the research field of high-entropy materials

was extended from alloys to other materials, including high-entropy ceramics, high-entropy polymers, and high-entropy composites [10]. In 2015, Rost et al. [11] reported for the first time a  $(\text{Mg}_{0.2}\text{Co}_{0.2}\text{Ni}_{0.2}\text{Zn}_{0.2}\text{Cu}_{0.2})\text{O}$  high-entropy oxide ceramics with five principal elements, which could solid-solve monoclinic CuO and hexagonal ZnO in a face-centered cubic crystal structure, which was different from the conventional solid-solution formation guidelines for oxide ceramics. This study demonstrated that high-entropy effects also exist in ceramic materials and successfully applied the high entropy concept formally to the study of oxide ceramics.

Entropy is a thermodynamic parameter that indicates a substance's chaotic state or degree of disorder. Entropy is affected by different configurations, including magnetic distance, atomic vibrations, and atomic ordering. For multi-major solid solutions, the stability is related to the Gibbs free energy  $G_{mix}$  [12]:

$$G_{mix} = H_{mix} - TS_{mix} \quad (1)$$

where  $H_{mix}$  is the enthalpy of the mixture,  $S_{mix}$  is the entropy of mixing, and  $T$  is the absolute temperature. As the entropy of mixing increases, the Gibbs free energy decreases, and the solid solution becomes more stable

\*Corresponding author:  
Tel : +86-159-4124-2356  
E-mail: lz19870522@126.com

[13, 14]. Since the entropy is affected by the temperature, the number of elements, and the atomic fraction of each element in the composition, the relationship between the mixing entropy  $S_{mix}$  of a multi-principal solid solution and the atomic fraction of each element can be expressed according to the Boltzmann entropy function equation:

$$S_{mix} = -R \sum_{i=1}^N x_i \ln x_i \quad (2)$$

In this equation,  $R$  is the gas constant,  $X_i$  is the atomic fraction of the  $i$ -th element, and  $N$  is the sum of elements. According to Eq. (2), when the number of elements is large enough and has the same atomic fraction, the mixed entropy of the multi-component solid solution will reach the maximum value [15]. From the entropy value, when the mixing entropy  $S_{mix} \geq 1.61R$  of the multi-element solid solution can be a high-entropy material, and this material has high stability. Akrami et al. [12] calculated the relationship between the entropy of mixing and the number of elements for multi-major element solid solutions (Fig. 1). They proposed a practical method to increase the entropy and stabilize medium/high-entropy materials. This entropy stabilization not only effectively improves the phase stability of single-phase materials but also contributes to the four major effects of high-entropy ceramics, including the thermodynamic high-entropy effect, structural lattice distortion effect, kinetic hysteresis-diffusion effect, and performance "cocktail" effect [16-20].

(1) Thermodynamic high-entropy effect: Theoretically, material systems of  $N$  elements can form up to  $N+1$  phases. However, high-entropy ceramics tend to form single-phase solid solutions. High-entropy ceramics have high configurational entropy due to their complex composition and disordered atomic distribution. According to the Gibbs free energy formula, the higher the entropy value, the lower the Gibbs free energy. Moreover, the Gibbs free energy will be even lower

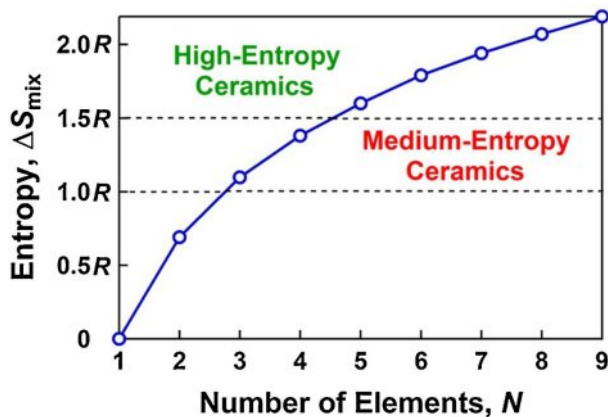


Fig. 1. Relation between entropy of mixing and number of elements and definition of medium-entropy ceramics and high-entropy ceramics [12].

under a high-temperature environment, which helps to promote the formation of a single-phase solid solution.

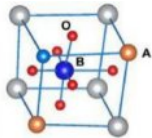
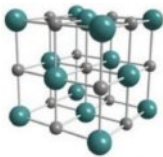
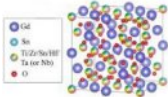
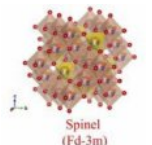
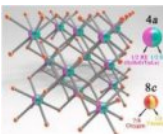
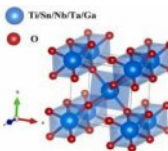
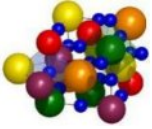
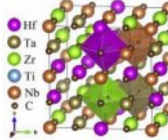
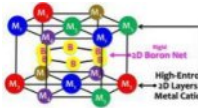
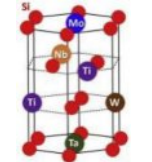
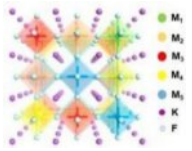
(2) Structural lattice distortion effect: Severe lattice distortions in high-entropy ceramics are due to different atomic sizes in the high-entropy phase. The atoms of various elements in high-entropy ceramics are randomly distributed in the crystal dot matrix, which can shift each lattice position due to the differences in radii and chemical bonds of different atoms. Therefore, the lattice distortion and defects of high-entropy ceramics will be more severe than those of conventional ceramics.

(3) Kinetic hysteresis-diffusion effect: Due to the lattice distortion effect of high-entropy ceramics, the diffusion activation energy of atoms inside the lattice increases, and the effective diffusion rate decreases. Therefore, elemental diffusion and phase transition rate within high-entropy ceramics is prolonged, and structural changes such as grain coarsening, recrystallization, and phase transition do not quickly occur under high-temperature conditions.

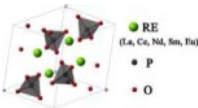
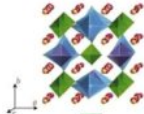
(4) Performance "cocktail" effect: High-entropy ceramics ultimately present properties that are not a simple, linear superposition of the fundamental properties of multiple components but rather the interaction and synergistic gain of multiple components, with a particular property sometimes exceeding the sum of the properties of all components. Unlike other core effects, the cocktail effect is neither hypothesized nor needs to be proven, it represents a special material effect.

Research on high-entropy ceramics with different compositions and structures has been continuously increasing in recent years. According to different compositions, high-entropy ceramics can be summarized as high-entropy oxide ceramics, high-entropy nitride ceramics, high-entropy carbide ceramics, high-entropy boride ceramics, high-entropy silicide ceramics, high-entropy fluoride ceramics, high-entropy phosphate ceramics, and high-entropy sulfide ceramics [21-29]. Among them, high-entropy oxide ceramics can be divided into perovskite structure, rock salt structure, pyrochlore structure, spinel structure, fluorite structure, and rutile structure according to their different structures (Table 1) [30-35]. High-entropy ceramics, as a new type of ceramics, have excellent mechanical properties, thermal insulation, corrosion resistance, energy storage, and conductivity performance. For example, high-entropy oxide ceramics with pyrochlore structure have lower thermal conductivity than YSZ ceramics in high-temperature environments, and their thermal expansion coefficient is also similar to NiCoCrAlY metal, so they are considered a promising ceramic material for thermal barrier coatings [36]; High-entropy boride ceramics and high-entropy nitride ceramics have high hardness, high strength, low thermal conductivity, and can further optimize their mechanical properties through second phase control [37, 38]. Therefore, applying high-entropy boride ceramics in the ultra-high temperature field has

**Table 1.** Main crystal structures of the high-entropy ceramics.

Category	Structure	Appearance	Composition	Characteristics	Reference
High-Entropy Oxide	Perovskite		$(\text{Bi}_{0.2}\text{Na}_{0.2}\text{Ba}_{0.2}\text{Sr}_{0.2}\text{Ca}_{0.2})\text{TiO}_3$	High energy recovery density and ultra-high efficiency	[39, 40]
	Rock-salt		$(\text{Co}_{0.2}\text{Cu}_{0.2}\text{Mg}_{0.2}\text{Ni}_{0.2}\text{Zn}_{0.2})_{1-x}\text{Li}_x\text{O}$	High dielectric constant and low dielectric loss	[41, 42]
	Pyrochlore		$(\text{Sm}_{0.2}\text{Eu}_{0.2}\text{Gd}_{0.2}\text{Dy}_{0.2}\text{Er}_{0.2})_2\text{Zr}_2\text{O}_7$	Low thermal conductivity, and excellent resistance to radiation damage	[43, 44]
	Spinel		$(\text{FeCoCrMnZn})_3\text{O}_4$	High discharge capacity and high conductivity	[45, 46]
	Fluorite		$(\text{Dy}_{0.2}\text{Ho}_{0.2}\text{Er}_{0.2}\text{Tm}_{0.2}\text{Lu}_{0.2})_2\text{Hf}_2\text{O}_7$	Low thermal conductivity and low coefficient of thermal expansion	[47]
	Rutile		$\text{TiSnNbTaGa}_2\text{O}_{12}$	Excellent microwave dielectric properties and high-temperature phase stability	[35]
High-Entropy Nitrides	NaCl-type		$(\text{HfNbTiVZr})\text{N}$	High hardness and good scratch resistance	[48, 49]
High-Entropy Carbides	Rock-salt		$(\text{HfTaZrTi})\text{C}$	Higher strength and stiffness, larger coefficient of thermal expansion, but poor ceramic toughness	[50]
High-Entropy Borides	$\text{AlB}_2$		$(\text{HfZrTiTaNb})\text{B}_2$	The Young's modulus and Vickers hardness are high, but the shear modulus is low, and there is a second phase containing Nb	[51, 52]
High-Entropy Silicides	$\text{CrSi}_2$ prototype		$(\text{Mo}_{0.2}\text{Nb}_{0.2}\text{Ta}_{0.2}\text{Ti}_{0.2}\text{W}_{0.2})\text{Si}_2$	High nano hardness and Vickers hardness, low thermal conductivity	[53]
High-Entropy Fluorides	Perovskite		$\text{K}(\text{MgCoNiCuZn})\text{F}_3$	Provides excellent catalytic activity for oxygen evolution reactions in alkaline media	[54]

**Table 1.** Continued.

Category	Structure	Appearance	Composition	Characteristics	Reference
High-Entropy Phosphates	Monazite-type		$(La_{0.2}Ce_{0.2}Nd_{0.2}Sm_{0.2}Eu_{0.2})PO_4$	Low thermal conductivity, and appropriate coefficient of thermal expansion	[55]
High-entropy sulfides	Cubic		$(HfZrTiTaNb)_2S_2$	High catalytic activity for oxygen evolution reaction and good stability	[56, 57]

received widespread attention.

In the application of high-entropy ceramics, the synthesis and sintering methods are the most important and central aspects. In the synthesis process, it is possible to change the microstructure of the material by adjusting the powder raw materials and process conditions, and to influence the degree of densification, grain size, grain distribution, grain boundaries, and internal stress of the ceramic material, which in turn affects the using properties of the ceramic material. In terms of sintering, the degree of densification of high-entropy ceramics has an important effect on their properties such as hardness, fracture toughness, and corrosion resistance. Therefore, when researching high-entropy ceramics, researchers often need to optimize the properties of the ceramics through various powder synthesis and sintering methods. The purpose of this paper is to review the advanced synthesis and sintering methods in the preparation of high-entropy ceramics, summarize the principles and technical flow of different processes, and discuss the current problems and future development directions.

### High-entropy Ceramic Synthesis Methods

Owing to their notable physical and chemical characteristics, including their elevated melting point, substantial hardness, exceptional mechanical attributes, and commendable resistance to corrosion, high-entropy ceramics have found extensive applications in industries demanding superior performance, such as metallurgy, refractory materials, precision cutting, cement manufacturing, aerospace engineering, and other technologically advanced sectors [58]. The synthesis of high-quality powder raw materials is a prerequisite for preparing high-performance and high-entropy ceramic materials. The purity, particle size, morphology, dispersion state, and other factors of powder raw materials significantly impact the physical and chemical properties of high-entropy ceramic materials [59]. The selection of a suitable powder synthesis route is based on the following aspects: the high-temperature phase stability of the powder, the uniform distribution of rare-earth elements inside the powder, the appearance and size of the powder, the properties, and application

scenarios [60].

### Solid-state reaction methods

The solid-state reaction method is the traditional method for synthesizing high-entropy ceramic powders. It is based on controlling the interdiffusion between the initial precursor powders to prepare high-entropy ceramic powders. The solid-state reaction is a chemical reaction involving the participation of solid-state substances. It refers to the process in which reactants, including solid-state substances, react for a certain period at a specific temperature to form the most structurally stable compounds by mutual diffusion of various elements [61]. At present, the solid-state reaction method used to prepare high-entropy ceramics is mainly a solid-solid-phase reaction. Due to the considerable bond strength between the atoms of different solid substances, the reaction rate is slow at room temperature, but through powder refinement, the temperature can be increased to enhance the transfer of heat between the substances and improve the reaction rate [62, 63].

The solid-state reaction method used to prepare high-entropy ceramics mainly consists of ball milling and high-temperature solid-state synthesis. For the lower melting point of ceramic powder raw materials, in the ball milling process, grinding balls, grinding jars, and inorganic material powder in the high-speed movement of mutual collision, shear, and friction, inorganic material powder in the strong impact and friction under the action of repeated extrusion, deformation, fracture and cold welding, and then through the enhanced hardening of the process for the synthesis of ceramic powder with a very fine microstructure [42]. The ceramic powder is continuously cold-welded, fractured, and refined to form many diffusion reactions while the diffusion distance is significantly shortened. Finally, the synthesis of high-entropy ceramic powder can be realized at room temperature [64]. Moskovskikh et al. [65] prepared two single-phase high-entropy carbide ceramic powders,  $(Hf_{0.2}Ta_{0.2}Ti_{0.2}Nb_{0.2}Zr_{0.2})C$  and  $(Hf_{0.2}Ta_{0.2}Ti_{0.2}Nb_{0.2}Mo_{0.2})C$ , by high-energy ball milling of Hf, Ta, Ti, Nb, Zr, Mo and graphite powders. Chicardi et al. [66] used Ti, Zr, Hf, V, Nb, Ta, and graphite powder as raw materials and passed 50-70 h of ball milling in an argon

atmosphere to synthesize six single-phase high-entropy carbide ceramics such as  $\text{TiZrHfVNbC}_5$ ,  $\text{TiZrHfVTaC}_5$  and  $\text{TiZrHfVTaC}_5$ .

The basic principle of the ball milling method is to use mechanical energy to induce chemical reactions or changes in the organization, structure, and properties of the material. This has the effect of significantly reducing the activation energy of the reaction, refining the grains, greatly improving the activity of the powder, and improving the uniformity of particle distribution [67]. In addition, the ball milling method can promote the diffusion of solid-state ions at low temperatures and retain ceramic materials' electrical and thermal properties, so applying this method to the synthesis of microwave-mediated high-entropy ceramics can effectively avoid dielectric property damage [68].

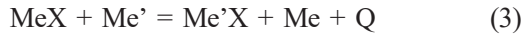
For oxide ceramic powders with high melting points, the heat generated during ball milling does not effectively activate the surface of the ceramic powders. Hence, ball milling is usually only used to achieve homogeneous mixing between different powders. Elemental diffusion between ceramic powders usually occurs during high-temperature solid-state synthesis after ball milling. The high-temperature solid-state method refers to the occurrence of interfacial contact between different kinds of powder particles in a high-temperature environment (1000-1500 °C) [69]. A chemical reaction occurs on the surface of powder particles in contact with each other, forming a new phase with fine organization and containing many structural defects. Finally, the structural adjustment and crystal growth of the new phase occur. In the high-temperature solid-state reaction, the factors affecting the solid-state reaction include the physicochemical properties of the powder feedstock and the powder morphology characteristics, including specific surface area, reactivity, and free energy change. Other influencing reaction conditions include reaction temperature, pressure, and additional environment [70, 71]. Zhu et al. [72] synthesized  $(\text{Nd}_{1/6}\text{Sm}_{1/6}\text{Eu}_{1/6}\text{Gd}_{1/6}\text{Dy}_{1/6}\text{Ho}_{1/6})\text{TaO}_4$ ,  $(\text{Nd}_{1/5}\text{Sm}_{1/5}\text{Eu}_{1/5}\text{Gd}_{1/5}\text{Dy}_{1/5})\text{TaO}_4$  and  $(\text{Nd}_{1/4}\text{Sm}_{1/4}\text{Eu}_{1/4}\text{Gd}_{1/4})\text{TaO}_4$  high-entropy ceramics by high-temperature solid-state reaction method using  $\text{RE}_2\text{O}_3$  (RE = Nd, Sm, Eu, Gd, Dy and Ho) and  $\text{Ta}_2\text{O}_5$ . The three ceramics prepared by this method have ferroelastic domains formed by a single-phase monoclinic structure and a square-monoclinic second ferroelastic phase transition. The presence of ferroelastic domains provides good mechanical properties ( $9.97 \pm 2.2$  GPa) as well as low thermal conductivity in high-temperature environments ( $2.98\text{-}1.23 \text{ W}\cdot\text{m}^{-1}\cdot\text{K}^{-1}$ , 100-1000 °C). Li et al. [73] used rare-earth oxide and  $\text{ZrO}_2$  as raw material powder, and prepared  $(\text{La}_{0.2}\text{Nd}_{0.2}\text{Sm}_{0.2}\text{Eu}_{0.2}\text{Gd}_{0.2})_2\text{Zr}_2\text{O}_7$  high-entropy ceramic by traditional solid-state reaction method, and the high-entropy ceramic demonstrated the highly sintering resistant and possess excellent thermal stability.

High-temperature solid-state synthesis has also been applied to the synthesis of dual-phase high-entropy

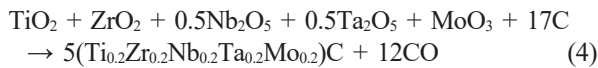
rare-earth zirconate ceramics. The dual-phase high-entropy ceramics are a newly developed ceramic structure in recent years, in which defects in the ceramic lattice are enhanced by elemental substitution in order to improve the thermophysical properties of the material [74]. Fan et al. [75] designed pyrochlore-fluorite dual-phase high-entropy rare-earth zirconates based on the average ionic radius ratio and the size disorder, and found that the formation of pyrochlore and fluorite dual-phase structures is more preferred when the ionic radius ratio ( $r_A/r_B$ ) is in the range of 1.4-1.5 and the size disorder parameter ( $\delta$ ) is higher than 5%. Yang et al. [76] found that the single-phase formation ability of high-entropy rare-earth zirconates depended on the cation radius difference and was independent of the entropy, and proposed the value of the cation radius difference of about 5.2% as a basis for predicting the formation of single- and dual-phase, which provided theoretical guidance for the preparation of dual-phase ceramics with good properties. Huang et al. [77] successfully prepared three kinds of high-entropy ceramics with different size disorder,  $(\text{La}_{0.25}\text{Nd}_{0.25}\text{Gd}_{0.25}\text{Yb}_{0.25})_2\text{Zr}_2\text{O}_7$ ,  $(\text{La}_{0.2}\text{Nd}_{0.2}\text{Sm}_{0.2}\text{Gd}_{0.2}\text{Yb}_{0.2})_2\text{Zr}_2\text{O}_7$ , and  $(\text{La}_{1/6}\text{Nd}_{1/6}\text{Sm}_{1/6}\text{Eu}_{1/6}\text{Gd}_{1/6}\text{Yb}_{1/6})_2\text{Zr}_2\text{O}_7$ , by high-temperature solid-state synthesis. Zhu et al. [78] prepared  $(\text{La}_{0.2}\text{Nd}_{0.2}\text{Y}_{0.2}\text{Er}_{0.2}\text{Yb}_{0.2})_2\text{Zr}_2\text{O}_7$  and  $(\text{La}_{0.2}\text{Nd}_{0.2}\text{Sm}_{0.2}\text{Gd}_{0.2}\text{Yb}_{0.2})_2\text{Zr}_2\text{O}_7$  high-entropy ceramics with dual-phase structure by high-temperature solid-state synthesis and compared the thermal conductivity with conventional single-phase high-entropy ceramics. The results showed that the dual-phase high-entropy ceramics had lower thermal conductivity compared with the single-phase high-entropy ceramics. This was due to the fact that the dual-phase structure was at the critical position of ordered and disordered phase transition, and there were more obvious lattice distortions as well as lattice relaxation phenomena inside its lattice. In addition, there were greater atomic mass and radius differences in the dual-phase ceramics, resulting in stronger phonon scattering from point defects within the dual-phase high-entropy ceramics.

### Thermal reduction

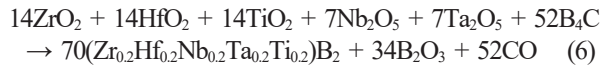
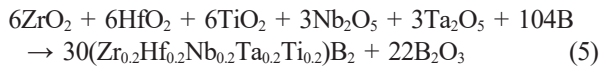
The thermal reduction method for synthesizing high-entropy ceramic powders involves using reducing agents to reduce the reactants, such as carbon (carbothermal reduction), boron (borothermal reduction), and boron carbide (borocarbothermal reduction) [79-81]. Before using the thermal reduction method to synthesize high-entropy ceramic powders, it is necessary to mix the reactants and reductants uniformly by mechanical means [82]. After that, the powders are heated to a certain temperature under a vacuum or inert gas environment so that the powder can produce a reduction reaction and a solid solution reaction and ultimately produce single-phase high-entropy ceramic powders [83]. The thermal reduction method can be expressed in terms of a general chemical Eq. (3):



In this formula, MeX generally represents the reduced oxide, Me' represents the thermal reducing agent, and Q represents the heat of the reaction. Feng et al. [84] synthesized high-entropy  $(\text{Hf}_{0.2}\text{Zr}_{0.2}\text{Ti}_{0.2}\text{Ta}_{0.2}\text{Nb}_{0.2})\text{C}$  powders with a single face-centered cubic structure by carbothermal reduction in a vacuum environment using transition metal oxides ( $\text{TiO}_2$ ,  $\text{ZrO}_2$ ,  $\text{Nb}_2\text{O}_5$ ,  $\text{Ta}_2\text{O}_5$ , and  $\text{MoO}_3$ ) and carbon powder as raw materials. The synthesized reaction formula for the powder is shown in Eq. (4).



Chen et al. [85] synthesized porous high-entropy  $(\text{Zr}_{0.2}\text{Hf}_{0.2}\text{Ti}_{0.2}\text{Nb}_{0.2}\text{Ta}_{0.2})\text{B}_2$  ceramics by borothermal reduction as well as borocarbothermal reduction, with synthetic reaction formulae shown in Eq. (5) and Eq. (6), respectively.



Based on the traditional carbothermal reduction method, Wu et al. [86] proposed a novel method of carbothermal reduction-melton calcium treatment, which was used to synthesize high-purity and high-entropy carbide powder. The specific process is as follows: Using transition metal oxides and excess carbon powder as raw materials, the metal oxides are first reduced to carbides by carbothermal reduction at lower temperatures. After that, the metal Ca is added to the carbides with free carbon and heat-treated. The Ca reacts with the free C to form  $\text{CaC}_2$  at high-temperatures, and the final product is acid-washed to remove the  $\text{CaC}_2$ . Currently, Wu et al. [87] have used this method for the synthesis of high-purity, high-entropy carbide powders such as  $(\text{Ti}_{0.2}\text{Zr}_{0.2}\text{Hf}_{0.2}\text{Nb}_{0.2}\text{Ta}_{0.2})\text{C}$ ,  $(\text{Zr}_{0.25}\text{Hf}_{0.25}\text{Nb}_{0.25}\text{Ta}_{0.25})\text{C}$ , and  $(\text{Ti}_{0.25}\text{Hf}_{0.25}\text{Nb}_{0.25}\text{Ta}_{0.25})\text{C}$ , which verified that the method was feasible in the synthesis of high-entropy ceramic powder.

Despite the many advantages of thermal reduction in synthesizing high-entropy ceramic powders, controlling the reductant content in the feedstock is crucial. For example, transition metal monocarbides used in carbothermal reduction methods generally have face-centered cubic crystal structures. It has been shown that carbides with face-centered cubic structures can rarely exist in ideal stoichiometric ratios and that carbon vacancies are widely present in the nonmetallic sublattices of transition-metal carbides, resulting in transition-metal carbides usually existing in nonstoichiometric

forms [88]. At present, further determination is needed regarding the effect of carbon content on the synthesis of high-entropy carbide powders. In addition, when synthesizing high-entropy carbons using carbothermal reduction, insufficient carbon in the feedstock leads to the presence of unreduced oxide impurities in the product, while excessive carbon leads to the presence of free carbon in the product, which is not conducive to the synthesis of high-purity powders. Therefore, the reducing agent's content needs to be precisely controlled before the preparation of high-entropy ceramic powders using the thermal reduction method.

### Self-propagating high-temperature synthesis

In the late 1960s, Borovinskaya et al. [89] first proposed the method of self-propagating high-temperature synthesis (SHS), which was used to prepare materials. After over 50 years of development, the self-propagating high-temperature synthesis method has been widely used to prepare powder materials, such as high-melting point ceramic powders, nanostructured alloy powders, and intermetallic compounds [90-92]. The self-propagating high-temperature synthesis method, also known as the combustion synthesis method, refers to a technology that synthesizes materials with a series of unique properties by self-heating and self-conducting effects under the condition of inert gas protection, utilizing external energy to induce a local chemical reaction in the reacting materials, and the heat of the released chemical reaction spreads to the immediately adjacent area and makes the reaction continue to take place [93]. During the synthesis process, the combustion reaction rate and transfer rate of the combustion wave is very rapid, generally 0.1-20.0 cm/s, and can reach a maximum of 25.0 cm/s. The combustion wave or reaction temperature is usually above 2100-3500 K and can reach 5000 K [93].

The reaction system for the self-propagating high-temperature synthesis of high-entropy ceramics can be a chemosynthesis reaction, a substitution reaction, or a decomposition complex reaction [94-96]. Regardless of the reaction system's form, the combustion-synthesis process is self-sustaining only if the heat generated by the reaction per unit mass burned is greater than the activation energy of the reactants. According to the laws of thermodynamics (Eq. (7)) [97].

$$\Delta G = \sum_{i=0}^n (\Delta H_{298}^0)_i - \sum_{i=0}^m (\Delta H_{298}^1)_i \quad (7)$$

In this formula,  $n$ ,  $m$ ,  $\Delta G$ ,  $\Delta H_{298}^0$ , and  $\Delta H_{298}^1$  represent the number of moles of the products, the number of moles of the reactants, the value of the standard Gibbs free energy change, the formation enthalpy of products at 298 K, the formation enthalpy of reactants at 298 K, respectively. Since most combustion synthesis is a highly exothermic reaction done instantaneously, with a short time for heat to propagate to the surrounding space, the

reaction system can be considered an adiabatic system. Under adiabatic conditions, the self-exothermic nature of the system leads to a gradual increase in the system temperature so that the amount of heat released at the start of the reaction can be expressed by Eq. (8) [97]:

$$Q_1^T = \int_{x=0}^T |\Delta H_T^r| dx \quad (8)$$

where  $x$  is the degree of reaction with time  $t$  at temperature  $T$ ;  $\Delta H_T^r$  is the change in reaction enthalpy at temperature  $T$ . When the reaction is carried out under adiabatic conditions, the reaction system entirely absorbs heat. It heats the whole reaction system to a temperature  $T$  when the total heat absorbed by the reaction system is [97]:

$$Q_2^T = \int_{x=0}^x \int_{T=T_0}^T \left( \sum_i n_i C_{pi} + \sum_k \int_{l=0}^l |\Delta H_k^m| dl \right) dx dT \quad (9)$$

where  $C_{pi}$  is the molar heat of component  $i$ ,  $n_i$  is the number of moles of component  $i$ ,  $\Delta H_k^m$  is the enthalpy of melting (transition) of component  $k$ ,  $l$  is the degree of melting of component  $k$  at  $(x, T)$ . When the entire reaction system gives off the same amount of heat as it absorbs at temperature  $T$ , the relationship between  $x$ ,  $T$  and  $l$  for a given reaction stage can be calculated from all the thermodynamic data. When the system is fully reacted, and  $x = l = 1$ , the maximum temperature  $T$  reached by the whole reaction system can be calculated, and this temperature is also made the adiabatic temperature ( $T_{ad}$ ). It is generally accepted that  $T_{ad}$  is the determining factor for self-propagating high-temperature synthesis and that the system is capable of self-sustaining combustion when  $T_{ad} \geq 1800$  K.  $T_{ad}$  and reaction rate can be adjusted in the following way [98-101]:

(1) Powder particle size and compaction density: Self-propagating high-temperature synthesis is a solid-phase reaction in which the reaction driving force is related to the contact area between the solid-phase particles. The smaller the powder particle size, the greater the diffusion of elements at the interface and the higher the peak temperature. Similarly, a higher billet density also increases the contact area between the powders, increasing the peak temperature and the reactivity.

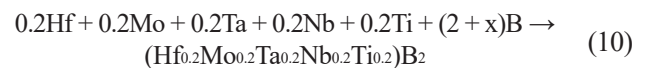
(2) Reaction material ratio: For synthetic reactions

with high combustion temperatures, changing the ratio of components in a chemical reaction can reduce the adiabatic value, and an excess of reactants or products usually reduces the reaction's exothermic heat and adiabatic temperature. Therefore, the  $T_{ad}$  can be lowered by adding a diluent.

(3) Initial ignition method: Since different initial ignition methods require different degrees of preheating, different amounts of heat released, and different areas of ignition, the degree of impurity introduction is different. This ultimately affects the rate and heat release of the reaction and changes the product morphology and particle size.

(4) Shielding gas pressure: The shielding gas pressure inhibits the expansion of the raw material during combustion and accelerates the combustion rate by improving the contact behavior between the powder particles. If the shielding gas does not participate in the reaction, the burning rate increases with the external pressure increase. It remains stable when the shielding gas pressure reaches a certain level.

The SHS preparation process has gradually matured in recent years, and its application in synthesizing high-entropy ceramic powders has increased. Nikolay et al. [102] carried out a self-propagating high-temperature synthesis under an argon environment using Hf-Ti-Cr-(Fe<sub>0.5</sub>V<sub>0.5</sub>) as the raw material according to the process in Fig. 2, and prepared the (Hf<sub>0.25</sub>Ti<sub>0.25</sub>Cr<sub>0.25</sub>(FeV)<sub>0.25</sub>)N high-entropy ceramics with a single-phase face-centered cubic crystal structure. Tallarita et al. [103] carried out a self-propagating high-temperature synthesis of Hf, Mo, Ta, Nb, Ti, and B in a closed argon environment and finally prepared (Hf<sub>0.2</sub>Mo<sub>0.2</sub>Ta<sub>0.2</sub>Nb<sub>0.2</sub>Ti<sub>0.2</sub>)B<sub>2</sub> high-entropy ceramic powders, with a reaction process as shown in Eq. (10):



The design of duplex composite high-entropy ceramics is one of the future development directions of new materials, and the thermodynamic properties of ceramic materials can be effectively improved by homogeneous doping of the second phase in high-entropy ceramics [104]. The self-propagation high-temperature synthesis method can achieve the homogeneous mixing of duplex

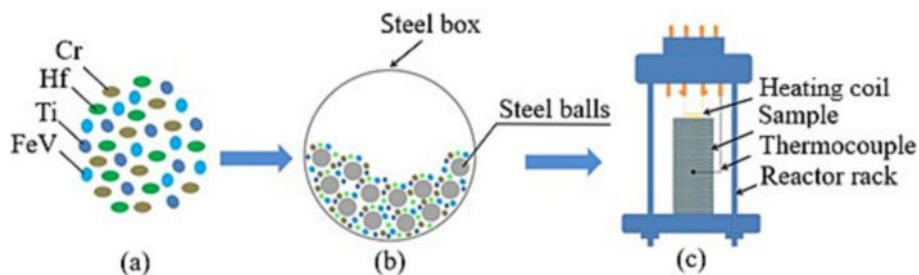
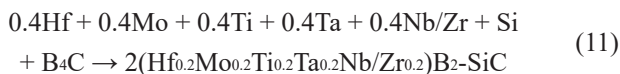


Fig. 2. Stages of obtaining of HEC material synthesis from Hf-Ti-FeV-Cr-N system [102].

composite high-entropy ceramics in the synthesis stage. Evseev et al. [105] performed a self-propagating high-temperature synthesis of Ti, C, Hf, and B in a nitrogen atmosphere. Finally, the HfTiCN duplex composite high-entropy ceramics containing 40 wt% TiB<sub>2</sub> second phase uniformly doped were prepared. Pakhomova et al. [106] combined the self-propagating high-temperature synthesis with the spark plasma sintering to prepare (Hf<sub>0.2</sub>Mo<sub>0.2</sub>Ti<sub>0.2</sub>Ta<sub>0.2</sub>Nb<sub>0.2</sub>)B<sub>2</sub>-SiC and (Hf<sub>0.2</sub>Mo<sub>0.2</sub>Ti<sub>0.2</sub>Ta<sub>0.2</sub>Zr<sub>0.2</sub>)B<sub>2</sub>-SiC duplex composite high-entropy ceramics. The reaction process is shown in Eq. (11).



After a long period of continuous development and research, the self-propagating high-temperature synthesis technology has made many breakthroughs in theory and practice, and its application in high-entropy ceramics synthesis has gradually increased. However, although the self-propagating high-temperature synthesis technology has the advantages of low energy consumption, simple process, and high product quality, the overly fast reaction process and large temperature gradient limit the development of this technology in the field of nanoscale high-entropy ceramic powder synthesis, for example, poor uniformity of the powder composition and non-uniformity of the powder particle size distribution [107]. Therefore, to optimize the application of self-propagating high-temperature synthesis technology in the synthesis of high-entropy ceramic powders, research should focus on the following aspects [108-110]: (1) Reduces adiabatic temperature by slowing down the combustion rate by adding diluents. Optimization of compositional uniformity and particle size distribution of high-entropy ceramic powders through reduction of combustion temperature gradient; (2) Optimization of the self-propagation process through a combination of processes, such as ball mill pretreatment, chemical furnace pretreatment, and modification of the reaction system; (3) Precise control of the reaction process is realized by combustion wave quenching and real-time XRD scanning; (4) Optimization of the control of high-entropy ceramic powder synthesis parameters through the continuous development of self-propagating sintering technology and the combination of thermochemical simulation and modelling.

### Sol-gel method

The sol-gel method originated in the 1860s when Graham et al. [111] discovered that the protosilicate tetraacetic acid produces glassy SiO<sub>2</sub> by hydrolysis under acidic conditions. The sol-gel method is a wet-chemistry process. In the typical process, metal salts or inorganic salts are dispersed into a solution for the hydrolysis-condensation reaction and then polymerized

into a gel at the appropriate temperature. The particle size distribution of the colloidal particles is controlled by adding a complexing agent such as ethylene glycol or citric acid. Ultimately, ceramic powders are prepared by calcining the cured gel at a specific temperature. The sol-gel method is based on the reaction between the alkoxide and the salt of metals to produce an oxide (Eq. (12)), and the process can be conducted in water (hydrolytic sol-gel) or under dry conditions (nonhydrolytic sol-gel) [112].



The alkoxide can be directly used for the oxide ceramics or it may be produced by an in-situ reaction between the salt of metals and ether or alcohol [112].



Modifying the synthesis parameters when preparing high-entropy ceramics using the sol-gel method can control the morphological characteristics of ceramic powders. Compared to solid-state reactions, the sol-gel method offers the following advantages [113-115]: (1) The raw materials used in the sol-gel method are first dispersed into the solvent and form a low-viscosity solution, so that homogeneous mixing of the raw materials can be achieved quickly. In particular, homogeneous mixing at the molecular level can be achieved between the reactants during the gel formation process; (2) After a reaction step in solution, homogeneous doping of trace elements at the molecular level can be achieved, and the elemental distribution can be optimized in high-entropy ceramics; (3) Chemical reactions will be easier to carry out and require lower synthesis temperatures than solid-phase reactions. It is generally accepted that the diffusion of components in a sol-gel system is in the nanometre range, whereas the diffusion of components in a solid-phase reaction is in the micrometer range, so the sol-gel method's reactions can be carried out at lower temperatures.

Fig. 3 shows the process of preparing ceramic powders using the sol-gel method [116]. Depending on the raw material, the chemical process can be divided into organic and inorganic processes. Depending on the sol-gel process, it can be classified into colloidal, inorganic polymers, and complexes. Specific characteristics are shown in Table 2.

Currently, the sol-gel method has been widely used for the preparation of high-entropy ceramic powders. Zhang et al. [117] successfully synthesized (La<sub>0.2</sub>Yb<sub>0.2</sub>Nd<sub>0.2</sub>Gd<sub>0.2</sub>Sr<sub>0.2</sub>)CrO<sub>3</sub> high-entropy ceramic powders with a single-phase orthorhombic chalcogenide crystal structure by the sol-gel method, and the average particle size of the powders was 800-1000 nm. Guo et al. [118] synthesized (La<sub>0.2</sub>Nd<sub>0.2</sub>Sm<sub>0.2</sub>Gd<sub>0.2</sub>Yb<sub>0.2</sub>)<sub>2</sub>



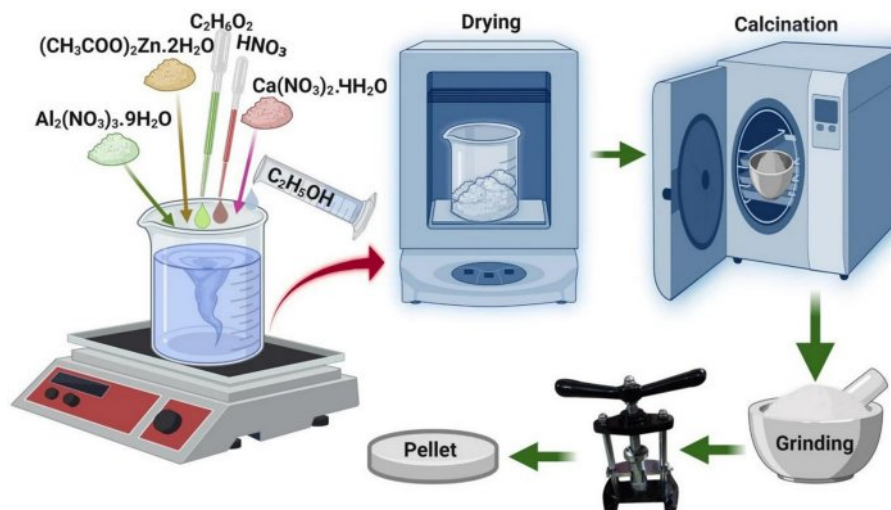


Fig. 3. Schematic diagram of ceramic powders prepared by sol-gel method [116].

Table 2. Characterization of different sol-gel processes.

Types	Precursor	Gel	Chemical characteristics
Colloid type	Metals, inorganic compounds, and additives	Gels are formed from dense particles. The gels have a high solid phase content and are transparent	Adjusting the pH or adding electrolytes to neutralize the charge on the particle surface
Inorganic polymer type	Metal hydrocarbon oxides	Inorganic polymers are formed from precursors and result in the formation of gels	Hydrolysis and polycondensation of precursors
Complex type	Metal alcohol salts, nitrates, acetates	Formation of gels through hydrogen-bonded complexes	Complexation reactions lead to the formation of complexes

$(Zr_{0.75}Ce_{0.25})_2O_7$  high-entropy ceramic powders by the sol-gel method. The powders have typical defective fluorite structures, and the average particle size of the powders is about 15 nm, which lays the foundation for high-performance high-entropy nano-structured materials for future application in thermal barrier coatings. Yang et al. [119] synthesized nanoscale  $(Hf_{0.2}Nb_{0.2}Cr_{0.2}Ta_{0.2}Mo_{0.2})B_2$  high-entropy boride ceramic powders by sol-gel method, and the synthesized powders have hexagonal single-phase structure and the average particle size reaches 62.09 nm. In addition, the synthesized single-phase high-entropy ceramic powders have a specific capacitance that is 27% higher than that of several powders, and the electrodes of high-entropy powders show 97.03% capacitance retention after 5000 cycles, which indicates that the sol-gel method can prepare high entropy boride ceramics with excellent electrochemical properties. Liu et al. [120] prepared  $(Sm_{0.2}Eu_{0.2}Tb_{0.2}Dy_{0.2}Lu_{0.2})_2Zr_2O_7$  high-entropy ceramic aerogels by combining the sol-gel method with the three-dimensional structural reconstruction technique after high-temperature calcination. By characterizing the ceramic aerogel's microstructure, thermal conductivity, and strength, researchers found that it has a typical nanoporous structure, a low thermal conductivity of only  $0.031 W \cdot m^{-1} \cdot K^{-1}$  (900 °C), and a strength of 12.95 MPa. Zhang et al. [121] utilized a combination of sol-gel

and ball milling to prepare  $(CuNiFeCoMg)_x-Al_2O_3$  high-entropy ceramics with a cubic phase and mesoporous structure, and this ceramic exhibited superior  $SO_2$  resistance in CO catalytic oxidation.

### Solution combustion synthesis

Solution combustion synthesis (SCS) is a technique for producing oxide nanopowders. This material synthesis technique is developed based on SHS [122]. Since the combustion temperature of the SHS method is usually between 2100 K and 3500 K, the higher reaction temperature imposes limitations on the product synthesis process and properties, making it difficult to realize the synthesis of ultrafine or nano-ceramic powders [123]. Therefore, the SCS method, which has a lower combustion temperature, has been developed. SCS is a violent redox reaction that combines wet-chemistry and combustion synthesis. Because its combustion temperature is low, it is also known as low-temperature combustion synthesis [124].

Solution combustion for the preparation of nanoceramic powders usually involves using metal nitrates as oxidizing agents and organic fuels as reducing agents [125]. The additions can be calculated based on propellant chemistry theory, in which the stoichiometric ratios are determined from the oxidizing agent's total oxidation valence and the

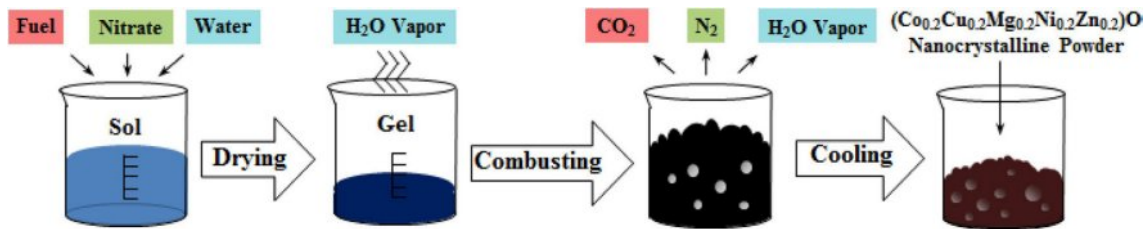


Fig. 4. Simplified scheme for the synthesis of  $(\text{Co}_{0.2}\text{Cu}_{0.2}\text{Mg}_{0.2}\text{Ni}_{0.2}\text{Zn}_{0.2})\text{O}$  by SCS method [128].

reducing agent's reduction valence in the reaction system. If the fuel content is more than the stoichiometric ratio, it is called a rich fuel system; less than the stoichiometric ratio is called a poor fuel system [126]. When the metal ions and organic fuels are in solution, after sufficient mixing, heating, evaporation, and concentration, the final solution foaming and combustion reaction at 150-500 °C environment. This process releases a large amount of gas due to decomposition, ultimately resulting in the formation of primary powder. This powder can be obtained in nanometer-scale ceramic form after appropriate temperature calcination [127].

Fig. 4 shows the flow chart of the solution combustion method for the preparation of high-entropy ceramic powder [128]. Metal nitrates and organic fuels are first mixed with water to prepare the sol.  $\text{NO}_3^-$  has better solubility in solution due to its excellent oxidizing ability and lower decomposition temperature. The homogeneously mixed solution was dried to produce a gel, after which the dried mixture was subjected in an elevated ambient environment to form a high-entropy ceramic powder. The combustion temperature can be estimated by the Eq. (15) [129]:

$$T_c = T_o + (\Delta H_r^o + \Delta H_p^o) / C_p \quad (15)$$

where  $T_o$ ,  $\Delta H_r^o$ ,  $\Delta H_p^o$ , and  $C_p$  are room temperature, formation enthalpy of reactants, formation enthalpy of products, and the heat capacity of the products at a constant pressure, respectively.

The solution combustion method for synthesizing high-entropy ceramic powders has several advantages compared to the solid-state reaction method [130-132]: (1) The solution combustion method has low requirements on equipment and process. Only the raw materials need to be configured into a solution, which is then ignited in the set way to prepare ultra-fine powder; (2) The reaction has low energy consumption and high efficiency. It can sustain itself with its own heat after ignition, without needing an additional heat source. The entire self-propagating reaction process can be completed within a few minutes; (3) The composition of the product is easily controlled, ensuring accurate stoichiometric ratio and homogeneity of the internal components of high-entropy ceramics at the molecular or atomic level; (4) Due to the rapid heating and cooling rates of the

reaction, non-equilibrium or metastable phases may form in the product, increasing its reactivity. Based on its numerous advantages, the solution combustion method is now widely utilized in synthesizing high-entropy ceramic powders. Cong et al. [133] used the solution combustion method to synthesize high-entropy ceramics with the composition  $(\text{Y}_{0.2}\text{Gd}_{0.2}\text{Dy}_{0.2}\text{Er}_{0.2}\text{Yb}_{0.2})_2\text{Hf}_2\text{O}_7$ . After examining the structure and properties, they discovered that the high-entropy ceramics had a single disordered fluorapatite structure, with the rare-earth cations evenly distributed in the ceramic powders. The thermal conductivity of the synthesized ceramics was only  $(0.73-0.93) \text{ W}\cdot\text{m}^{-1}\cdot\text{K}^{-1}$ , which was significantly lower than that of traditional YSZ. Zuo et al. [134] synthesized  $(\text{Sr}_{0.6}\text{Bi}_{0.2}\text{Na}_{0.2})(\text{Ti}_{0.75}\text{Zr}_{0.125}\text{Al}_{0.0625}\text{Nb}_{0.0625})\text{O}_3$  high-entropy ceramics with a single-phase chalcogenide structure using the solution combustion method. The ceramics demonstrated a high recoverable energy density of  $\sim 4.46 \text{ J}/\text{cm}^3$  at a high critical electric field of 520 kV/cm, a high energy efficiency of  $\sim 88.52\%$ , a large power density of  $\sim 176.65 \text{ MW}/\text{cm}^3$  (at 400 kV/cm), and an ultrafast discharge time of  $\sim 48 \text{ ns}$ . This research confirmed that the solution combustion method could be used for the synthesis of high-performance high-entropy dielectric ceramic powders. Cong et al. [135] synthesized  $(\text{La}_{0.2}\text{Ce}_{0.2}\text{Pr}_{0.2}\text{Sm}_{0.2}\text{Eu}_{0.2})_2\text{Hf}_2\text{O}_7$  ceramics with a single-phase ordered pyrochlore structure using solution combustion. This ceramic had highly homogeneous in composition at the nanometer and micrometer scales, excellent phase stability at 1600 °C, as well as demonstrated a low thermal conductivity  $(1.0-1.24 \text{ W}\cdot\text{m}^{-1}\cdot\text{K}^{-1})$  which was lower than those of rare-earth hafnates. Gautam et al. [136] developed a sol-gel self-combustion method by combining the sol-gel method with the solution combustion method. The synthesis of the high-entropy rock salt phase  $(\text{CoCuMgNiZn})\text{O}$  typically requires annealing at 850 °C. However, the sol-gel self-combustion method allows the synthesis of single-phase structured rock salt  $(\text{Co}_{0.2}\text{Cu}_{0.2}\text{Mg}_{0.2}\text{Ni}_{0.2}\text{Zn}_{0.2})\text{O}$  high-entropy ceramics at a lower temperature of 185 °C.

The solution combustion method has made significant progress after years of research and has become an essential way to prepare high-entropy ceramic powders. However, a few issues still need to be addressed in the solution combustion method [137, 138]: (1) It's challenging to precisely control the solution combustion process, and it's important to thoroughly investigate the mechanism

of synthesizing high-entropy ceramic powders using this method; (2) The powder products tend to agglomerate easily, affecting the homogeneity and stability of the powder particles; (3) It's difficult to accurately control the characteristics of powder size, morphology, and crystalline shape on the nanometer scale. Therefore, it is crucial to enhance the solution combustion method by integrating it with other technologies to gain better control over the size, morphology, and crystal shape of high-entropy ceramic powder. The development of environmentally friendly synthetic methods for large-scale production is a significant focus for future research.

### Co-precipitation method

The main mechanism of the co-precipitation method is to use a specific chemical reaction to make metal ions co-precipitate with precipitant to realize the purification, enrichment, and effective use of metal elements, and finally to obtain high-entropy ceramic powder through different heat treatment methods [139]. The specific preparation steps are as Fig. 5 [140, 141]: First, the metal chloride or nitrate is dissolved in deionized water to form a salt solution; Then an appropriate amount of chemical precipitant is added, resulting in a co-precipitation reaction; Ultimately, high-entropy ceramic materials can be obtained through washing, drying, calcination, and other subsequent processes. The preparation of high-entropy ceramics by co-precipitation method has many advantages, such as simple experimental principle, convenient operation, easy batch production, and product collection. In addition, by changing the test parameters such as solution pH, reaction temperature, and nature of precipitant, the regulation of product properties, morphology, and size can be realized.

The mechanism of preparing nanoscale high-entropy ceramic powders by co-precipitation can be illustrated

by the growth mechanism of the powders during the synthesis process [142]. Typically, the synthesis of high-entropy ceramics involves two processes, including the uniform nucleation of monomers with a critical size and the growth of multiple crystal nuclei. According to the schematic growth mechanism of Lamer's theory, the nucleation and growth process of high-entropy ceramics can be divided into three stages: In the first stage, the concentration of the components gradually increases to the over-saturation state, and there is no nucleation in this stage; In the second stage, when the monomer concentration is over-saturated to a certain degree, a large number of nucleation begins, and the component concentration decreases sharply to the critical nucleation concentration; In the third stage, when the concentration between the saturation concentration and the critical nucleation concentration, the concentration of the component remains stable, at which time the nucleation process stops and the grain growth stage begins [143].

Luo et al. [144] prepared  $(\text{Ce}_{0.2}\text{Nd}_{0.2}\text{Sm}_{0.2}\text{Eu}_{0.2}\text{Yb}_{0.2})_2\text{Zr}_2\text{O}_7$  high-entropy ceramics by reverse co-precipitation method using  $\text{CeCl}_3$ ,  $\text{Nd}_2\text{O}_3$ ,  $\text{Sm}_2\text{O}_3$ ,  $\text{Eu}_2\text{O}_3$ ,  $\text{Yb}_2\text{O}_3$ , and  $\text{ZrOCl}_2 \cdot 8\text{H}_2\text{O}$  as raw materials. They dissolved the rare-earth oxide powder in nitric acid to form a nitrate solution, while  $\text{ZrOCl}_2 \cdot 8\text{H}_2\text{O}$  and  $\text{CeCl}_3$  were dissolved in deionized water, and these solutions were mixed to form a homogeneous mixed solution containing all the desired elements. The mixed solution was slowly added dropwise to the  $\text{NH}_4\text{OH}$  while stirring continuously to ensure a homogeneous reaction. Under alkaline conditions, metal ions in the solution will combine with hydroxide ions to form a mixed hydroxide precipitate. Ultimately, high entropy ceramic powder was obtained through precipitate treatment and high-temperature calcination.

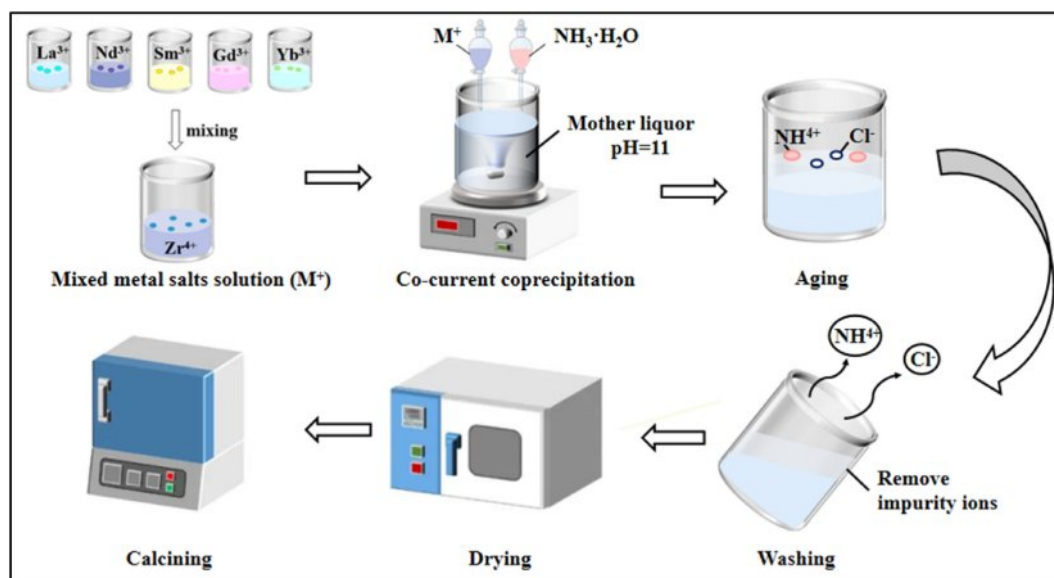


Fig. 5. Synthesis route diagram of  $\text{Ln}_2\text{Zr}_2\text{O}_7$  and  $\text{RE}_2\text{Zr}_2\text{O}_7$  ceramic powders [141].

### Hydrothermal synthesis

The hydrothermal method is to use the water sealed in the container as the medium, at a certain temperature and pressure, to make the normal temperature and pressure insoluble in water substances dissolved and chemical reaction or recrystallization reaction. Ultimately, the reaction product over-saturates precipitation and yields the nanoceramic material [145].

Since the hydrothermal method is a wet chemical synthesis completed in a closed vessel, it differs from the sol-gel method mainly in terms of temperature and pressure. Hydrothermal methods are usually used at temperatures between 130-250 °C, and the corresponding vapor pressure of water is 0.3-4 MPa [146]. The advantages of ceramic powder prepared by hydrothermal synthesis can be summarized as follows: (1) Under hydrothermal conditions, the ions can react according to the stoichiometry, and the grains can grow following the crystallization habit to produce perfect crystals; (2) The ceramic powders prepared by hydrothermal method have excellent performance compared to powders prepared by other methods, which is mainly demonstrated in the complete development of the powder grains, the particle size distribution is narrow, and the degree of agglomeration is light; (3) The hydrothermal production process is relatively simple and avoids the agglomeration of powders, the introduction of impurities, and structural defects that occur during high-temperature scorching and ball milling [147-149].

With the improvement of the current equipment manufacturing technology, the hydrothermal synthesis technology has been very mature and widely used in the powder synthesis and preparation of high-entropy ceramics. In recent years, the hydrothermal method has become an important method for the preparation of regular morphology high-entropy ceramic powders. Sun et al. [150] synthesized  $(\text{Bi}_{0.2}\text{Na}_{0.2}\text{Ba}_{0.2}\text{Ca}_{0.2}\text{Sr}_{0.2})\text{TiO}_3$  (BNBCST) high-entropy ferroelectric ceramics by hydrothermal synthesis method with high-pressure heating of the suspension at 200 °C. The innovation of synthesizing high-entropy ferroelectric ceramics by this method was that NaOH solution not only provided a solvent environment, but also could be used directly as a Na source and mineralizer for high-entropy ceramics, which avoided the use of an additional Na source and provided a high-purity powder synthesis route. However, the ceramic powders synthesized using the hydrothermal method showed a multiphase structure (Fig. 6), and since BNBCST was considered to be a solid solution formed by  $\text{Bi}_{0.5}\text{Na}_{0.5}\text{TiO}_3$ ,  $\text{BaTiO}_3$ ,  $\text{CaTiO}_3$ , and  $\text{SrTiO}_3$ , it was assumed that there existed  $\text{Bi}_{0.5}\text{Na}_{0.5}\text{TiO}_3$ ,  $\text{BaTiO}_3$ ,  $\text{CaTiO}_3$ , and  $\text{SrTiO}_3$  in the multiphase product. This result confirmed that it is difficult to realize the preparation of single-phase high-entropy ceramics by hydrothermal method.

Yu et al. [151] analyzed the effect of hydrothermal reaction temperature (120-220 °C) on the composition

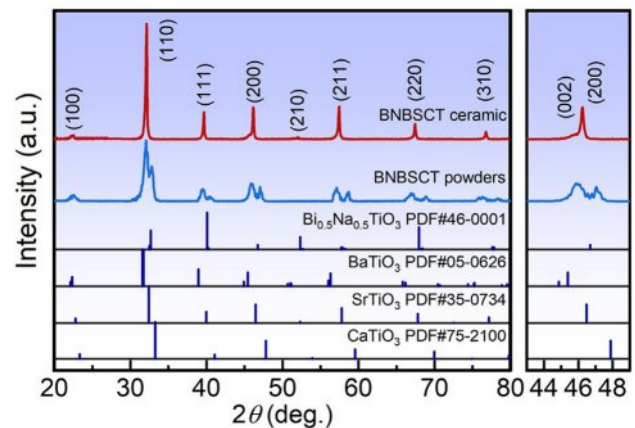


Fig. 6. XRD patterns of hydrothermal-synthesized BNBCST powders and HECs sintered at 1200 °C [150].

of  $(\text{Ba}_{0.2}\text{Mg}_{0.2}\text{Ca}_{0.2}\text{Sr}_{0.2}\text{Pb}_{0.2})\text{TiO}_3$  high-entropy ceramic phases. The results showed that when the temperature was in the 100-120 °C range the high-entropy oxide powder was a single phase. However, the  $\text{Pb}_5\text{O}_8$  impurity phase appeared in the powder product in the temperature range of 120-220 °C, and the diffraction peaks of the lead oxide phase increased with the increase in reaction temperature.

### Nebulized spray pyrolysis

Nebulized spray pyrolysis originated in the 1950s and has been successfully applied to the preparation of MgO ceramic powders [152]. After decades of continuous improvement, this method is widely used in the preparation of metal alloy powders, ceramic powders, organic-inorganic composite powders, and other materials [153]. Due to the features of high purity, homogeneous composition, and excellent micro-morphology of the ceramic powder produced by using this method, and the simple production process of this method, which can realize one-step molding and large-scale mass production, this method is regarded as a high-entropy ceramic powder synthesis technology with great application prospects [154-156].

The process of preparing ceramic powders by nebulized spray pyrolysis is shown in Fig. 7 [157]. Compared with synthesis methods based on conventional batch reactions (solid-state reaction, sol-gel, and co-precipitation), nebulized spray pyrolysis is a powder synthesis technique with relatively simple equipment, and its advantages mainly include the following aspects [158-160]: (1) The raw materials of high-entropy ceramics can be uniformly distributed in the solution, and the stoichiometric ratio between the rare-earth components can be precisely controlled through calculation, which effectively reduces the amount of tests needed to explore the ratio between the components; (2) The raw material droplets are suspended in the atmosphere after atomization, and various physicochemical reactions can

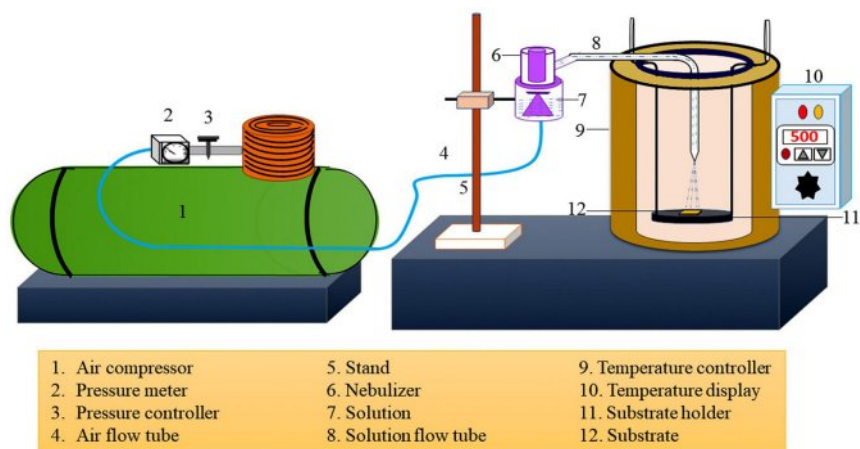


Fig. 7. Schematic diagram of nebulizer spray pyrolysis setup [157].

be completed in a very short time, which reduces the possibility of agglomeration between the nanopowder particles, and the final formation of the high-entropy ceramic powder exists in the form of hollow spherical particles and effectively avoids the influence of the purity and activity of the product in the mid-stage and late-stage milling process; (3) The droplets can realize the formation of high-entropy ceramic powders with different microstructures and thermophysical properties by controlling the concentration of precursor solution, solution flow rate, gas flow rate and decomposition temperature and other parameters during the reaction process; (4) The process equipment is relatively simple, without special requirements for the vacuum degree of the environment, and the one-step molding process does not require subsequent filtration, washing, drying, grinding, and other complex processes, which reduces the opportunity for the doping of impurity elements and is conducive to improving the purity of the powder.

The nebulized spray pyrolysis technique has great potential for application in both industrial and laboratory studies due to its unique advantages. With the continuous research and improvement of the nebulized spray pyrolysis technique, researchers have applied this method to the powder synthesis of high-entropy ceramics. Saker et al. [161] prepared  $(\text{Gd}_{0.2}\text{La}_{0.2}\text{Nd}_{0.2}\text{Sm}_{0.2}\text{Y}_{0.2})(\text{Co}_{0.2}\text{Cr}_{0.2}\text{Fe}_{0.2}\text{Mn}_{0.2}\text{Ni}_{0.2})\text{O}_3$  high-entropy ceramics by nebulized spray pyrolysis. They continuously delivered a water-based solution containing appropriate equiatomic cation combinations into a piezo-driven nebulizer, where particles were formed by flowing oxygen into a hot-wall reactor at 1050 °C and a pressure of 900 mbar. The generated mist containing fine droplets of the precursor solution was conveyed to a hot-wall reactor, where the synthesized particles were collected using a filter-based collector and calcined at 1200 °C for 2 h in air atmosphere with a heating/cooling rate of 10 °C·mm<sup>-1</sup>. Ultimately, the prepared high-entropy ceramics had a single perovskite structure and the powder morphology was a spherical hollow agglomerate with an average

particle size of 180 nm.

Flame spray pyrolysis is a new material preparation technology developed based on nebulized spray pyrolysis technology [162]. By spraying the precursor solution to form an aerosol and introducing it into a high-temperature flame, the solvent is rapidly evaporated and triggers the thermal decomposition of the metal salts, and then the solid state is precipitated due to over-saturation, and ultimately nano-scale or micron-scale ceramic powders are obtained [163]. This technological process not only includes a series of physicochemical processes such as solvent evaporation, solute precipitation to form solid particles, particle drying, thermal decomposition of particles, and sintering densification, but also can be performed at high temperatures and in vacuum environments [164].

The advantages of flame spray pyrolysis include its simple process, low production cost, and the ability to rapidly realize the synthesis and preparation of nanopowders [165]. During the preparation process, the precursors undergo decomposition, nucleation, solidification, sintering, agglomeration, and cooling in a very short period. Compared with nanomaterials prepared by conventional methods, the sintering behavior of flame spray pyrolysis at high temperatures and the effect of loading on the surface activity of ceramic powders have unique characteristics, including non-porous powder surface morphology, easy-to-control powder crystallinity, excellent high-temperature stability, and product reproducibility [166, 167]. Therefore, the researchers applied this technique to the synthesis and preparation of high-entropy powders.

Phakatkar et al. [168] prepared  $(\text{Mn}_{0.18}\text{Fe}_{0.16}\text{Ni}_{0.18}\text{Cu}_{0.28}\text{Zn}_{0.19})_3\text{O}_4$  high-entropy oxide nanoparticles (HEO NPs) by flame spray pyrolysis. They used anhydrous ethanol as a solvent and dissolved equimolar metal salts of Mn, Fe, Ni, Cu, and Zn in ethanol solution for the preparation of metal salt precursor solutions. The preparation process is shown in Fig. 8(a). To achieve the homogeneously mixed precursor solution, the solution was continuously

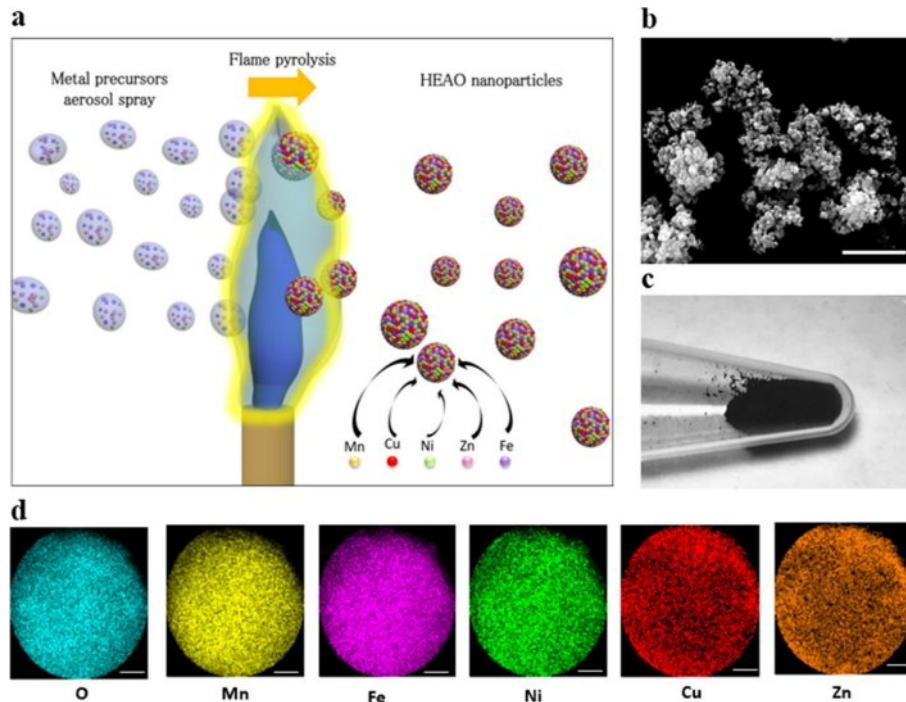


**Fig. 8.** (a) Schematic representation of HEO NPs synthesis by the FSP route; (b) SEM micrograph of the synthesized HEO NPs; (c) Digital photograph of as-synthesized HEO NPs; and (d) STEM-EDS mapping of single HEO nanoparticle [168].

stirred for 3 h at 700 rpm, and successive 20 min of ultrasonication was used. The twinfluid nozzle with air-assisted external mixing capability was utilized to generate the aerosol droplets. The compressed air was used as the atomizing gas. The precursor solution flow rate was 5 mL/min. The precursor solution aerosol droplets were directed through the propane torch flame at 1900 °C. Fig. 8(b)-(d) shows the powder morphology and elemental distribution, which confirmed that the elements were uniformly distributed inside the nanopowder, and the nanoceramic powder with a hollow structure was successfully prepared.

Sarkar et al. [169] prepared (Co, Cu, Mg, Ni, Zn)O and (Co, Mg, Ni, Zn)O high-entropy oxides by flame spray pyrolysis. They atomized the precursor solution in a compressed air atomizer and the mist formed was carried by oxygen into the flame. Since the residence time of the mist in the flame was very short, thus rapid heating, thermal decomposition/pyrolysis, and quenching of the powder particles occurred in the flame. Ultimately, ceramic powders with a particle size distribution of  $10 \pm 2$ - $73 \pm 32$  nm were obtained.

### High-entropy Ceramic Sintering Methods

In the preparation process of high-entropy ceramics, sintering is also the most crucial step. In the sintering process, with the temperature increases and time extends, the powder particles in the ceramic blanks are bonded to each other, the grain size increases, and the sample is transformed from a loose and porous structure

to a homogeneous and dense structure. Finally, it becomes a polycrystalline sintered body with complex characteristics. The densification level of high-entropy ceramics significantly impacts their hardness, fracture toughness, corrosion resistance, and thermomechanical properties. The sintering process of high-entropy ceramics exhibits complex densification characteristics due to the hysteresis diffusion effect. Efforts are being made to develop efficient sintering processes for high entropy ceramics to reduce production energy consumption and shorten the sintering cycle.

### Solid-state sintering

Solid-state sintering is the most common and well-established method used in the preparation of ceramics. The sintering method involves placing the ceramic green body into a conventionally heated furnace and using conventional heating to complete the densification of the sample at high temperatures [170].

The densification process of solid-state sintering consists of three stages [171]: The initial stage of solid-state sintering consists of a certain degree of sintering neck formation between the ceramic particles, and the contact area between the particles increases from zero to an equilibrium state. The contribution of the initial stage of sintering to the densification of the ceramic green body is small, generally less than 10% [172]. The theoretical models for the initial stages of solid-state sintering were based on the two-sphere model and assumed that the change in the center distance between the two spheres was equal to the linear shrinkage of the sintered body

[173]. Under this assumption, mass transfer processes such as surface diffusion, vapor-phase evaporation, and volumetric diffusion are assumed not to contribute to the linear shrinkage of the sintered body. In contrast, viscous flow, interfacial diffusion, and volumetric diffusion in the sintering neck are considered to reduce the center distance between particles and improve densification [174]. The middle stage of sintering starts at the beginning of grain growth and is accompanied by the extensive formation of intergranular interfaces, but the pores are still interconnected and form a continuous network, while the intergranular crystalline interfaces still exist in a mutually independent state [171]. Most of the densification process and some of the microstructural changes arise in this stage, thus the middle stage of sintering contributes the most to the densification [175]. As the pores become independent during sintering and the grain boundaries begin to form a continuous network, the sintering enters the latter stages. At this stage the freestanding pores are often located at the grain interfaces or may be encapsulated in the grains. In the latter stages, the rate of ceramic bulk densification slows down significantly, however, the grain growth is more rapid [171, 176].

Li et al. [177] prepared high-entropy ceramics of  $(\text{La}_{0.2}\text{Nd}_{0.2}\text{Sm}_{0.2}\text{Eu}_{0.2}\text{Gd}_{0.2})_2\text{Zr}_2\text{O}_7$  with pyrochlore structure by solid-state sintering. They analyzed the synthesis temperature of  $(\text{La}_{0.2}\text{Nd}_{0.2}\text{Sm}_{0.2}\text{Eu}_{0.2}\text{Gd}_{0.2})_2\text{Zr}_2\text{O}_7$  by XRD, and found that the diffraction peaks of the sintered samples showed a single-phase pyrochlore structure when the sintering temperature was increased to 1000 °C, which proved that this compositional high-entropy ceramic could be synthesized at 1000 °C. As the sintering temperature increased to 1500 °C, the half peak width of the (400) diffraction peak decreased and the crystallinity of the sample increased. Qin et al. [178] successfully prepared Nb-Ta-Ti-Zr-Ce-Hf-Sc-Y-La-Pr-Nd-Sm-Eu-Gd-Tb-Dy-Ho-Er-Tm-Yb-Lu-O high-entropy ceramics using the solid-state sintering method by holding the ceramic green body at 1600 °C for 24 h. Moreover, weberite and fergusonite phases and a pyrochlore-weberite transformation appeared for the first time in this high-entropy ceramic.

Solid-state sintering is the simplest and most common method for the preparation of ceramics, but to obtain dense ceramics, it is necessary to hold them at high temperatures for a long period, which can easily lead to grain coarsening. To reduce the grain growth rate during solid-state sintering, the researchers proposed a two-step sintering method based on solid-state sintering [179]. After the first step of holding the ceramic bulks at a high temperature for a short time to achieve the required densities, the second step of holding the ceramic bulks at a lower temperature for a long time to avoid excessive grain growth and obtain relatively dense samples. Yu et al. [180, 181] prepared  $(\text{Hf}_{0.2}\text{Zr}_{0.2}\text{Ta}_{0.2}\text{Nb}_{0.2}\text{Ti}_{0.2})\text{C}$  high-entropy carbide ceramics using solid-state sintering and

two-step sintering, respectively. The solid-state sintering process was held at 2200 °C for 2 h, and the two-step sintering process was reduced to  $T_2=1900$  °C and held for 8 h after the temperature reached  $T_1=2200$  °C. Compared with the solid-state sinter samples, the two-step sintered samples showed a decrease in the average grain size from 7.00 μm to 6.19 μm, and a decrease in the average pore size from 0.90 μm to 0.75 μm.

The preparation of high-entropy ceramics using traditional solid-state sintering requires a long time of sintering at high temperatures to complete the densification of the ceramic samples, and it consumes a large amount of energy and time to achieve the desired results. Therefore, the development of more efficient and energy-saving sintering technology has great significance for the research and application of high-entropy ceramics.

### Spark plasma sintering

Spark plasma sintering (SPS), also known as plasma-activated sintering or pulsed current sintering, is a rapid sintering process that has been researched since the 1990s [182]. In this process, high-frequency pulsed currents pass directly between the molds and powder particles or in the block samples, generating plasma discharges between the powder particles. This leads to the rapid sintering and densification of the ceramic green body, facilitated by the combined effects of a local high-temperature field, electric field, and pressure field [183]. Spark plasma sintering technology is a process that combines plasma activation, hot pressing, and resistance heating. It offers several advantages such as uniform heating, high heating rate, low sintering temperature, short sintering time, and high productivity [184]. This technology can achieve surface purification of ceramic powder particles, inhibit grain growth, and create a homogenous and controllable structure [185]. In comparison to vacuum hot press sintering, spark plasma sintering is cost-effective and straightforward. Additionally, the sintering process can be promoted using DC pulse voltage based on Joule heat and powder plastic deformation [186].

The SPS device's basic structure is illustrated in Fig. 9 [187]. It primarily consists of a pressure system, vacuum system, water cooling system, temperature measurement system, power supply, and control system. During the SPS sintering process, the on/off pulse current generates a significant amount of heat as it passes through the mold and powder [188]. Additionally, due to the gaps between the ceramic powder particles within the powder blanks, spark discharges occur between adjacent particles, ionizing some of the gas molecules. The positive ions and electrons resulting from ionization move toward the cathode and anode, respectively, and discharge between the particles to form a plasma. As the plasma density increases, the high-speed movement of the particle flow on the surface of the ceramic powder produces a significant spark impact, removing adsorbed gases from the powder surface [189]. This process activates

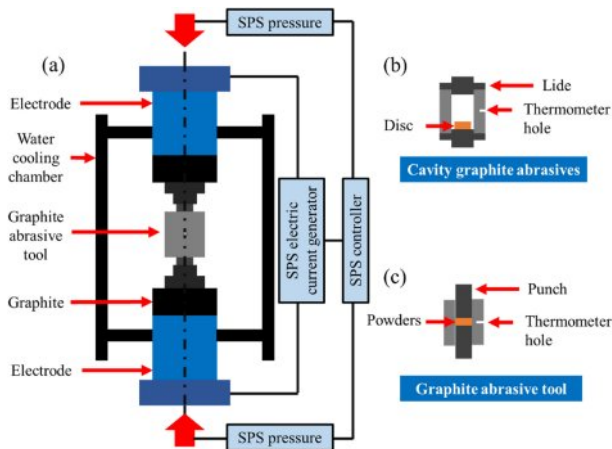


Fig. 9. Schematic diagram of spark plasma sintering [187].

the particle surfaces, promoting material migration and achieving rapid sintering.

The procedure of spark plasma sintering for sintering high-entropy ceramic green bodies is shown in Fig. 10. Before performing the specific SPS, the specimen is first loaded into a graphite mold, which is then placed between the upper and lower electrodes. The specimen underwent pressurization using an oil pressure system, followed the cavity was evacuated using a vacuum pump. Once the sintering environment reached the required vacuum level, a pulsed current was applied to the graphite abrasive tool. The pulsed current is applied directly to the conductive mold and the sample [190]. A portion of the current passing through the sample causes partial discharges between the sample's pores and generates plasma, while another portion passing through the mold heats the mold and transfers heat to the ceramic green body. The specimen begins to shrink as the temperature rises, and the degree of shrinkage increases with the extension of the sintering time. Until the contraction ends after reaching the sintering temperature, the ceramic green body densification reaches its maximum [191].

Since the pulsed current voltage applied for sintering can provide high-density energy for sintering and form

a diffuse motion of the discharge point, the edge of the ceramic powder particles can instantly form a high-temperature field under the action of the pulsed electric field and achieve the rapid sintering of the ceramic billet under the action of pressure [192]. Based on the above characteristics, the researchers applied the spark plasma sintering technology to sintering high-entropy ceramic materials with the hysteretic diffusion effect. Zhang et al. [193] prepared high-entropy  $(Y, Gd, Sm, Eu, Dy)_3Fe_5O_{12}$  garnet ceramics by SPS. The results indicate that SPS can significantly reduce the sintering temperature ( $1100\text{ }^\circ\text{C}$ ) and sintering time (3 min) of high-entropy garnet ceramics. Moreover, the high-entropy garnet ceramics have superior thermal expansion stability and leaching resistance compared with conventional garnet ceramics. Lu et al. [194] prepared  $(Bi_{0.2}Na_{0.2}Sr_{0.2}Ba_{0.2}Ca_{0.2})TiO_3$  lead-free relaxation ferroelectric ceramics using conventional sintering as well as spark plasma sintering, respectively, and compared the effects of different sintering methods on the properties of dielectric ceramics. The ceramics prepared using the conventional sintering method exhibited a polarization value of  $34.9\text{ }\mu\text{C}/\text{cm}^2$ , an energy storage density of  $2.53\text{ J}/\text{cm}^3$ , and an energy storage efficiency of  $56.8\%$  under an electric field of  $250\text{ kV}/\text{cm}$ . In contrast, the ceramics prepared with SPS demonstrated a higher polarization of  $57.2\text{ }\mu\text{C}/\text{cm}^2$ , an energy storage density of  $6.66\text{ J}/\text{cm}^3$ , and an energy storage efficiency of  $77.2\%$  at an electric field of  $430\text{ kV}/\text{cm}$ . The enhanced performance of the SPS samples can be attributed to their high density, refined grains, number of oxygen vacancies, and compositional homogeneity within the samples. Chen et al. [195] prepared  $(La_{1/7}Nd_{1/7}Sm_{1/7}Eu_{1/7}Gd_{1/7}Dy_{1/7}Ho_{1/7})_2Zr_2O_7$  using SPS by setting the sintering temperature, pressure and the time to  $1600\text{ }^\circ\text{C}$ ,  $16\text{ kN}$  uniaxial pressure and 3 min, respectively. The results showed that the relative density, nanoindentation hardness, and fracture toughness of the sintered samples reached  $97.72\%$ ,  $13.86\text{ GPa}$ , and  $1.1\text{ MPa}\cdot\text{m}^{1/2}$ , respectively, which were much higher than those of the conventional single-component sintered pyrochlore structural ceramics.

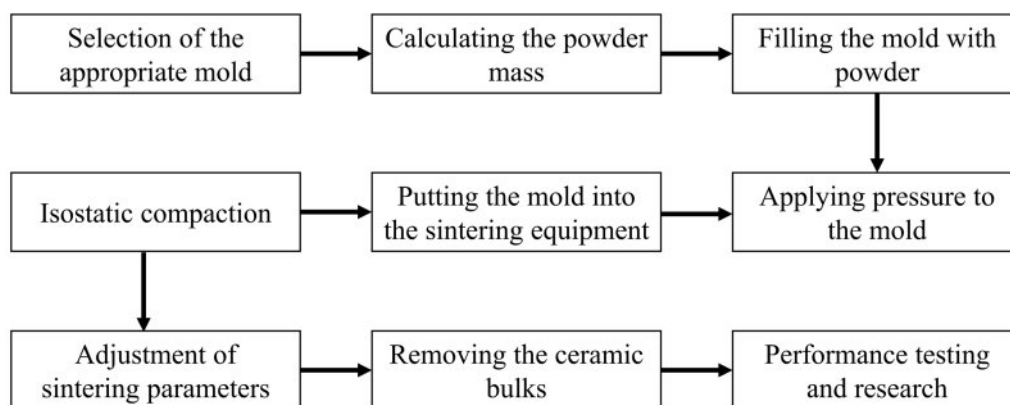
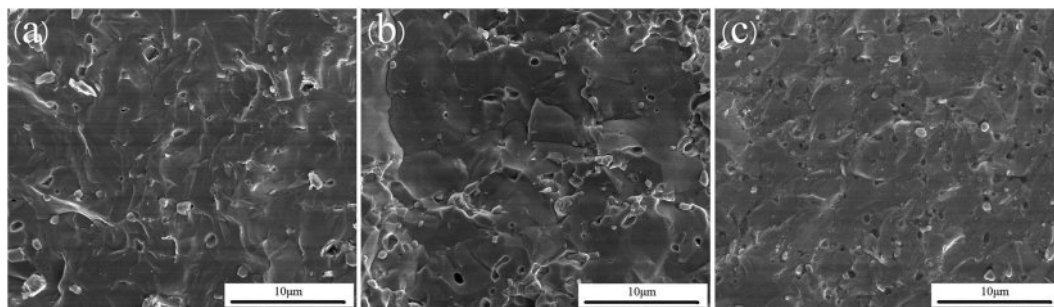


Fig. 10. Procedure of spark plasma sintering for sintering high-entropy ceramic green bodies.





**Fig. 11.** Fractured surface SEM images of the as-fabricated ceramics after SPS at 2000 °C: (a)  $(\text{Hf}_{0.2}\text{Zr}_{0.2}\text{Ta}_{0.2}\text{Cr}_{0.2}\text{Ti}_{0.2})\text{B}_2$ , (b)  $(\text{Hf}_{0.2}\text{Mo}_{0.2}\text{Zr}_{0.2}\text{Nb}_{0.2}\text{Ti}_{0.2})\text{B}_2$ , and (c)  $(\text{Hf}_{0.2}\text{Mo}_{0.2}\text{Ta}_{0.2}\text{Nb}_{0.2}\text{Ti}_{0.2})\text{B}_2$  [197].

The research on high-entropy boride ceramics started in 2016, it is difficult to achieve sintering densification due to the hysteresis diffusion effect and impurity influence of high-entropy materials. Gild et al. [196] prepared high-entropy boride ceramics  $(\text{Hf}_{0.2}\text{Zr}_{0.2}\text{Ta}_{0.2}\text{Nb}_{0.2}\text{Ti}_{0.2})\text{B}_2$  for the first time by high-energy ball milling method and spark plasma sintering. They densified the ceramic green bodies using spark plasma sintering at 2000 °C, 30 MPa, and 5 min after high-energy ball milling and cold isostatic pressing of the mixed powders. The results of the compositional analysis showed that the sintered blocks had a uniform internal distribution of metal elements without segregation and a relative density of 92–93%. The preparation of high-entropy boride ceramics with the same composition using hot-press sintering needed to be held at 1800 °C for 1 h to obtain dense samples. Compared with hot press sintering, the spark plasma sintering technique reduced the sintering time, but the sintering process needed to be optimized to obtain denser samples.

Zhang et al. [197] combined the borothermal reduction with the spark plasma sintering to prepare  $(\text{Hf}_{0.2}\text{Zr}_{0.2}\text{Ta}_{0.2}\text{Cr}_{0.2}\text{Ti}_{0.2})\text{B}_2$ ,  $(\text{Hf}_{0.2}\text{Mo}_{0.2}\text{Zr}_{0.2}\text{Nb}_{0.2}\text{Ti}_{0.2})\text{B}_2$ , and  $(\text{Hf}_{0.2}\text{Mo}_{0.2}\text{Ta}_{0.2}\text{Nb}_{0.2}\text{Ti}_{0.2})\text{B}_2$  three dense high-entropy boride ceramics by 10 min sintering at 2000 °C and 30 MPa. Fig. 11 shows the cross-sectional morphology of the three high-entropy ceramics, the relative density of the  $(\text{Hf}_{0.2}\text{Zr}_{0.2}\text{Ta}_{0.2}\text{Cr}_{0.2}\text{Ti}_{0.2})\text{B}_2$  ceramics was 99.2% and the hardness was  $(28.3 \pm 1.6)$  GPa. On this basis, Zhang et al. [198] combined borocarbothermal reduction and spark plasma sintering to prepare  $(\text{Hf}_{0.2}\text{Zr}_{0.2}\text{Ta}_{0.2}\text{Nb}_{0.2}\text{Ti}_{0.2})\text{B}_2$ ,  $(\text{Hf}_{0.2}\text{Zr}_{0.2}\text{Mo}_{0.2}\text{Nb}_{0.2}\text{Ti}_{0.2})\text{B}_2$ , and  $(\text{Hf}_{0.2}\text{Mo}_{0.2}\text{Ta}_{0.2}\text{Nb}_{0.2}\text{Ti}_{0.2})\text{B}_2$  high-entropy boride ceramics. Compared with the high-entropy ceramics previously prepared by borothermal reduction, the high-entropy ceramic powders obtained by borocarbothermal reduction were characterized by higher purity, and the densities of  $(\text{Hf}_{0.2}\text{Mo}_{0.2}\text{Zr}_{0.2}\text{Nb}_{0.2}\text{Ti}_{0.2})\text{B}_2$  and  $(\text{Hf}_{0.2}\text{Mo}_{0.2}\text{Ta}_{0.2}\text{Nb}_{0.2}\text{Ti}_{0.2})\text{B}_2$  were increased from 97.7%, 95.0% to 98.1%, 98.5%, respectively.

High-entropy carbide ceramics also suffer from the problem of difficult sintering. Ye et al. [199] investigated the synthesis conditions of  $(\text{Hf}_{0.2}\text{Zr}_{0.2}\text{Ta}_{0.2}\text{Nb}_{0.2}\text{Ti}_{0.2})\text{C}$  by the first principle calculations and found that the

ceramic green bodies could be sintered at 1800 °C and 30 MPa for 30 min to obtain ceramic bulks with a relative density of 95.3%. Yan et al. [200] prepared  $(\text{Hf}_{0.2}\text{Zr}_{0.2}\text{Ta}_{0.2}\text{Nb}_{0.25}\text{Ti}_{0.2})\text{C}$  by spark plasma sintering, and sintering the ceramic green bodies at 2000 °C and 30 MPa for 10 min to obtain ceramic bulks with the relative density of 93%. The performance test results showed that the high-entropy carbide ceramics had excellent performance in thermal conductivity, electrical conductivity, and mechanical properties compared with HfC, ZrC, TaC, and TiC.

Castle et al. [201] used spark plasma sintering to prepare  $(\text{HfTaZrTi})\text{C}$  and  $(\text{HfTaZrNb})\text{C}$  high-entropy carbide ceramics. They investigated the effect of sintering time on high-entropy carbide ceramics by subjecting the ceramic green bodies to spark plasma sintering at 2300 °C for 2 min, 5 min, and 10 min, respectively. At 2 min of sintering, the relative density of  $(\text{HfTaZrNb})\text{C}$  ceramics was 94% and the elemental distribution was inhomogeneous; at 5 min of sintering, the relative density increased to 97% and the EDS results showed that the elemental inhomogeneity still existed; at 10 min of sintering, the relative density of the ceramic blocks reached 98% and the elements were uniformly distributed, but chemical decomposition occurred in the ceramic blocks, forming two rock salt structural phases. Finally, they set the sintering time at 7 min and kept the samples at 1800 °C for 10 min before spark plasma sintering, and obtained high-entropy carbide ceramics with high hardness, high purity, and high hardness.

Spark plasma sintering technology has been widely used in the preparation and sintering of high-entropy ceramics. Compared with hot-press sintering, although spark plasma sintering does not reduce the sintering temperature, it significantly promotes the synthesis and densification process of high-entropy ceramics and reduces the sintering time to a few minutes [202]. Currently, the spark plasma sintering still has some limitations. The first one is the microscopic mechanism of the current effect during the sintering process is not clear. If the effects of the electric field on powder surface cleaning and material sintering kinetics can be determined, more precise parameter control during the

sintering process can be performed to obtain superior material properties. The second is that the spark plasma sintering is a near-net-shape process, carbon molds will lead to the unqualified surface smoothness of the ceramic bulks or contamination by carbon. Therefore, the future development of mold materials will improve the spark plasma sintering. The third is the limitations of the sample shape, the current spark plasma sintering samples are prepared mainly for simple cylinders, and it is difficult to prepare ceramic green bodies with complex shapes, which cannot satisfy the needs of the actual engineering. In addition, in the process of developing new molds, it is necessary to consider the densities and tissue uniformity at different locations. Therefore, the development of diversely shaped ceramics is the future of spark plasma sintering.

### Flash sintering

Flash sintering is a highly prospective sintering process for the rapid densification of ceramic powders [203]. Flash sintering is an electric field-assisted sintering technology that rapidly densifies ceramic powders through the combined effects of the electric field, current, and temperature [204]. Flash sintering has its own characteristics compared to SPS, mainly in terms of current conduction and heat generation mechanisms [205, 206]: (1) In terms of current conduction, spark plasma sintering relies heavily on the more conductive graphite mold for current flow. In flash sintering, current is forced to flow from one end of the specimen to the other; (2) In terms of the mechanism of heat generation, spark plasma sintering achieves the heating of ceramic powder through thermal radiation and heat conduction, while flash sintering generates Joule heat through electric current and forms a small amount of liquid phase inside the ceramic powder, and ultimately obtains the densified sintered blocks through liquid-phase sintering and solid-state sintering.

Fig. 12 illustrates the flash sintering device structure, including the sintering furnace, displacement sensor, DC or AC power supply, electrode material, and multimeter

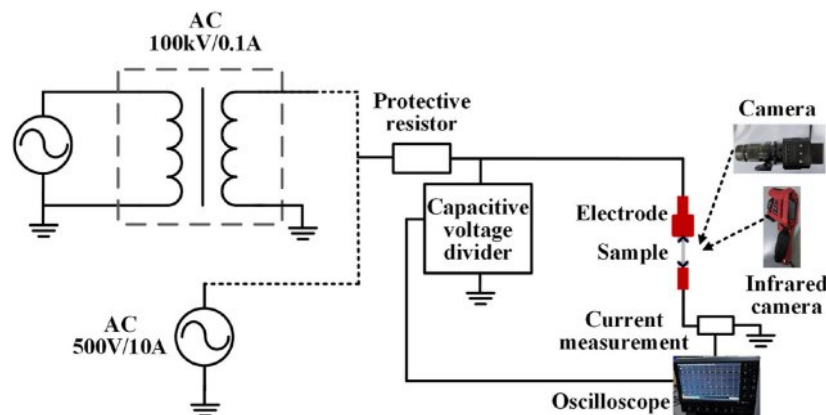


Fig. 12. Schematic diagram of the experimental platform [207].

[207]. Compared to spark plasma sintering, flash sintering is more designable. This includes the shape of the ceramic green body and customization of the sintering equipment [208, 209]: (1) In terms of the shape of the ceramic green body, researchers have used strips, rods, and bone-shaped specimens for sintering. A simple flash sintering unit can be set up by connecting electrodes to the ends of the specimen and then connecting the electrodes to an external power supply; (2) In terms of sintering equipment, for sintering that needs to be accomplished at a suitable temperature condition, tube or box furnaces can be used to heat the green body to the desired initial temperature; For samples that can be flash sintering at low temperatures, a heating plate can be used in place of the high-temperature furnace, and for samples that can be flash sintering in a room-temperature environment, the heating device can be eliminated. In addition, researchers can also add thermocouples, infrared thermometers, optical cameras and other components to realize real-time monitoring of the sintering process. It can be seen that flash sintering has a broader scope for equipment enhancement compared with spark plasma sintering.

Fig. 13 shows the variation curves of current, voltage, power loss, and other parameters over time in the flash sintering process [210]. Generally, the flash sintering process can be divided into three stages: gestation, mutation, and steady-state [211]. In the gestation stage, with the increase in temperature, the resistivity of the sample gradually decreases, and the current through the sample gradually increases; In the mutation stage, the resistivity and voltage of the sample suddenly decrease, and the current and power loss increase dramatically; In the steady state stage, the current, voltage and power loss of the sample enter into a stable state. Compared with conventional sintering methods, the most apparent advantage of flash sintering is the substantial reduction of sintering temperature and the significant reduction of sintering time. Flash sintering is a rapid ceramic sintering process that can complete the sintering of ceramic samples in just a few minutes or even seconds. This

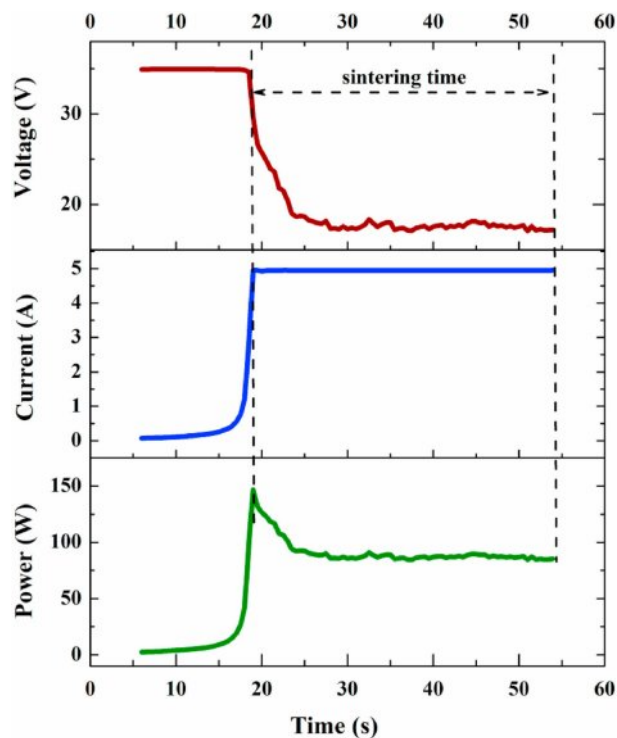


Fig. 13. Variation of voltage, current, and the power dissipation of the circuit during the FS process [210, 211].

method allows the furnace temperature to be lowered by several hundred degrees Celsius, effectively preventing the ceramic green body from being exposed to high temperatures for extended periods. As a result, it helps to avoid issues such as coarse grain formation, making it a promising high-entropy ceramics sintering technique with great potential for practical application.

In 2020, Kumar et al. [212] first synthesized the high-entropy oxide  $\text{Mg}_{0.2}\text{Ni}_{0.2}\text{Co}_{0.2}\text{Cu}_{0.2}\text{Zn}_{0.2}\text{O}$  by flash sintering. They applied an electric field of  $100 \text{ V}\cdot\text{cm}^{-1}$  to a ceramic green body at a furnace temperature of  $350^\circ\text{C}$  and flash sintering for 3 min at a preset current to obtain samples with densities above 90%. In addition, they investigated the effect of current on the sintered samples. When the sintering currents were set to 600 mA, 700 mA, and 900 mA, the sintered samples were all single-phase rock salt structure and had relative densities of 92%, 93%, and 95%, with an increase in the average size of the grains from 400 nm for 600 mA to a value of 1–2  $\mu\text{m}$  for 900 mA, respectively.

Liu et al. [213] prepared high-entropy oxide  $\text{Mg}_{0.2}\text{Ni}_{0.2}\text{Co}_{0.2}\text{Cu}_{0.2}\text{Zn}_{0.2}\text{O}$  ceramics using flash sintering. The ceramic green bodies were flash sintering at  $25^\circ\text{C}$ , electric field strength of  $250 \text{ V}\cdot\text{cm}^{-1}$ , and a current density of  $80 \text{ mA}\cdot\text{mm}^{-2}$  for 1 min, and a further reduction of the sintering temperature was realized. In addition, they investigated the effect of current density on the phase transformation of the ceramics during the flash sintering process. The XRD results showed that the flash sintering samples were in a multi-phase mixed state when the

current density was  $70 \text{ mA}\cdot\text{mm}^{-2}$ , and the flash sintering samples were in a single-phase rock salt structure when the current density was increased to  $80 \text{ mA}\cdot\text{mm}^{-2}$ . On this basis, Li et al. [214] prepared  $\text{Ca}_{0.2}\text{Co}_{0.2}\text{Ni}_{0.2}\text{Cu}_{0.2}\text{Zn}_{0.2}\text{O}$  ceramics by room temperature reactive flash sintering and compared them with solid-state sintering samples. The reaction flash sintering was carried out at  $25^\circ\text{C}$  with an electric field strength of  $60 \text{ V}\cdot\text{cm}^{-1}$ , and several groups of samples were flash sintering for 30 s by applying current densities of  $100 \text{ mA}\cdot\text{mm}^{-2}$ ,  $200 \text{ mA}\cdot\text{mm}^{-2}$ , and  $300 \text{ mA}\cdot\text{mm}^{-2}$ , respectively. The XRD results showed that the flash sintering samples with a current density of  $300 \text{ mA}\cdot\text{mm}^{-2}$  exhibited a single-phase rock salt structure, while the solid-state sintering samples still had some CaO and did not fully synthesize the single-phase rock salt high-entropy ceramics.

Ma et al. [215] prepared  $(\text{MgCoNiCuZn})_{1-x}\text{Li}_x\text{O}$  ( $x=0, 0.10, 0.15, 0.20,$  and  $0.30$ ) high-entropy oxide ceramics by flash sintering and investigated the optimal current density for flash sintering of materials with different compositions and the effect of flash sintering on the electrical properties of the materials. The results showed that the optimal sintering current density of the undoped high-entropy oxide ceramics was  $210 \text{ mA}\cdot\text{mm}^{-2}$ , while the optimal sintering current density of the Li-doped high-entropy oxide ceramics was  $735 \text{ mA}\cdot\text{mm}^{-2}$ . During solid-state sintering, oxidation of  $\text{Co}^{2+}$  occurred in the undoped high-entropy oxide ceramics. During the reactive flash sintering of Li-doped high-entropy ceramics, the charge imbalance was compensated by holes and oxygen vacancies in the valence band of the oxides, and the formation of more oxygen vacancies leads to an increase in the ionic conductivity with the increase in Li concentration.

Wang et al. [216] prepared high-entropy perovskite ceramics  $\text{Sr}(\text{Ti}_{0.2}\text{Y}_{0.2}\text{Zr}_{0.2}\text{Sn}_{0.2}\text{Hf}_{0.2})\text{O}_{3-x}$  by flash sintering for 1 min at a furnace temperature of  $1000^\circ\text{C}$  and a current density of  $40 \text{ mA}\cdot\text{mm}^{-2}$ . Compared with solid-state sintering, the sintering time for the synthesis of single-phase high-entropy oxides using flash sintering was reduced from 10 h to 1 min, and the sintering temperature was lowered from  $1500^\circ\text{C}$  to  $1314^\circ\text{C}$ , which makes flash sintering highly advantageous for the rapid synthesis of high-entropy oxides. However, the relative density of the flash sintering samples was about 70%, and subsequent optimization of the current density or sintering time was needed to obtain dense ceramic bodies.

High-entropy ceramics with a pyrochlore structure have low thermal conductivity and excellent high-temperature phase stability, which make them highly potential materials for thermal barrier coatings and superior host phase for the long-lived radionuclide in nuclear waste. However, solid-state sintering is difficult to obtain dense high-entropy pyrochlore ceramics and requires prolonged sintering in high-temperature environments. Zhao et al. [217] synthesized high-entropy

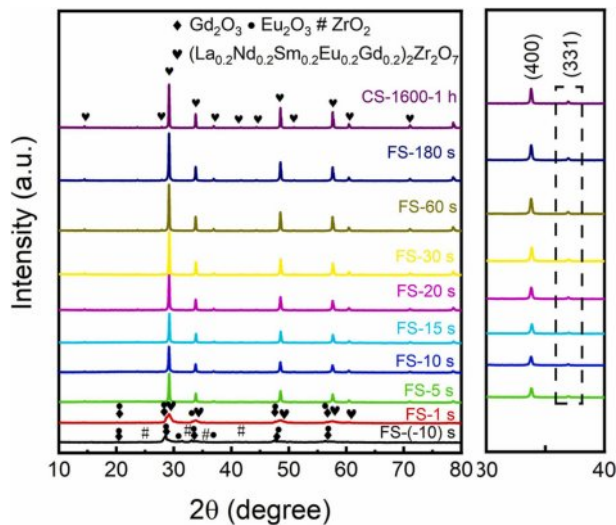


Fig. 14. XRD patterns of flash sintered samples and conventional pressurelessly sintered samples [217].

pyrochlore ceramics  $(\text{La}_{0.2}\text{Nd}_{0.2}\text{Sm}_{0.2}\text{Eu}_{0.2}\text{Gd}_{0.2})_2\text{Zr}_2\text{O}_7$  by reactive flash sintering and characterized the phase transformation process, densification behavior, and grain growth process of high-entropy ceramics during the flash sintering process. The results are shown in Fig. 14. The samples consisted of a mixture of the original oxides and a minimal high-entropy ceramics before 10 s of the flash sintering started; at the beginning of 1 s of the sintering, most of the samples had formed high-entropy ceramics but a small amount of oxides still existed; when the sintering time was prolonged to 5 s, the original oxides had been wholly transformed into  $(\text{La}_{0.2}\text{Nd}_{0.2}\text{Sm}_{0.2}\text{Eu}_{0.2}\text{Gd}_{0.2})_2\text{Zr}_2\text{O}_7$ ; when the flash sintering time continued to be prolonged to 180 s, the crystallinity of the samples increased, and the diffraction peaks of high-entropy ceramics became more sharp. According to crystal growth kinetics calculations, the flash sintering densification rate was 60 times that of solid-state sintering, while the grain growth rate was only 1.5 - 6 times that of solid-state sintering.

Mao et al. [218] successfully prepared high-entropy pyrochlore ceramics  $(\text{La}_{0.2}\text{Nd}_{0.2}\text{Sm}_{0.2}\text{Eu}_{0.2}\text{Gd}_{0.2})_2\text{Zr}_2\text{O}_7$  by reaction flash sintering for 1 min at 1200 °C, electric field strength  $9 \text{ V}\cdot\text{mm}^{-1}$  and applied pressure 10 MPa. The effects of different current densities on the relative density, hardness, and Young's modulus of ceramic blocks were investigated and compared with the solid-state sintering samples sintered at 1600 °C for 3 h and 6 h. The results showed that when the current density was increased from  $60 \text{ mA}\cdot\text{mm}^{-2}$  to  $200 \text{ mA}\cdot\text{mm}^{-2}$ , the average grain size of the ceramic blocks increased from  $0.6 \mu\text{m}$  to  $2.4 \mu\text{m}$  and the relative density increased from 91 % to 99 %. However, the relative density of the solid-state sintering samples was 97%, which was lower than that of the flash sintering samples at  $200 \text{ mA}\cdot\text{mm}^{-2}$ , and the average grain size of the solid-state sintering samples was  $5.2 \mu\text{m}$ , which was a larger increase in the average

grain size than that of the flash sintering samples. In terms of mechanical properties, the flash sintering samples had better hardness and fracture toughness.

In summary, compared with solid-state sintering, the applied electrical field of flash sintering facilitates the material diffusion and densification process, which not only shortens the sintering time of high-entropy ceramics from several hours to several minutes or even tens of seconds but also significantly reduces the sintering temperature and effectively suppresses the excessive growth of grains. The flash sintering technique, as a new type of high-entropy ceramic sintering method, has shown excellent sintering results in practical applications. However, the research on the micro-mechanism of sintering is still insufficient, and the shape of the ceramic green bodies used for sintering is mainly in the dog-bone shape, so the research and design of the sample shape, electrode shape, electrode type, and the rate of temperature rise and fall are the future development direction.

### Oscillatory pressure sintering

For a long time, material defects such as porosity, microcracks, and agglomerates have been the primary factors limiting the strength and reliability of ceramic materials [219]. The advancement in ceramic sintering equipment and sintering technology is crucial for overcoming this challenge. Oscillating pressure sintering is based on hot press sintering and transforms a constant pressure into an oscillating pressure, which can be programmed in both size and frequency [220]. In 2014, Xie et al. [221] proposed the use of dynamic oscillating pressure with controllable frequency and amplitude, based on constant static pressure, to achieve coupled dynamic pressure sintering during the ceramic powder sintering process. In the early stage of sintering, the oscillating pressure helps the powder rearrange and increases the packing density of the original powder; In the middle stage of sintering, the oscillating pressure can provide a greater driving force for powder sintering, which is more conducive to promoting grain slip, plastic deformation, and diffusive mass transfer phenomena in the sintered body [222].

In 2021, Li et al. [223] first prepared high-entropy ceramics using oscillatory pressure sintering and investigated the crystal structure, microstructure, and thermal conductivity of the sintered samples. High-entropy boride  $(\text{Zr}_{0.2}\text{Ta}_{0.2}\text{Nb}_{0.2}\text{Hf}_{0.2}\text{Mo}_{0.2})\text{B}_2$  ceramics were subjected to oscillatory pressure sintering for 1h at 1900 °C and 25-35 MPa. The prepared ceramic samples had a relative density of 96.6%, a typical hexagonal structure, and a Vickers hardness of  $24.0\pm 1.0 \text{ GPa}$ , with significantly improved mechanical properties over the SPS samples. In terms of thermal performance,  $(\text{Zr}_{0.2}\text{Ta}_{0.2}\text{Nb}_{0.2}\text{Hf}_{0.2}\text{Mo}_{0.2})\text{B}_2$  had a thermal conductivity of  $12.2 \text{ W}\cdot\text{m}^{-1}\cdot\text{K}^{-1}$  at room temperature, which was much lower than that of conventional boride ceramics.

Oscillatory pressure sintering technology can continue to provide sufficient sintering driving force in the later stages of sintering, further enhance the densification of the material, and improve the properties, such as flexural strength and hardness. The research related to the preparation of high-entropy ceramics by oscillating pressure sintering is still in the early exploratory stage, and the established research has shown that the oscillating pressure has an obvious promotion effect on the particle rearrangement and movement in the process of high-entropy ceramics densification. In the preparation of dense high-entropy ceramics, oscillatory pressure sintering has an advantage that cannot be ignored.

### Microwave sintering

Microwave sintering uses the dielectric loss of ceramic materials in the microwave electromagnetic field, making the ceramic green body to the sintering temperature and complete the densification [224, 225]. Microwave is an electromagnetic wave with a wavelength between 1 mm and 1 m, and a frequency between 300 MHz and 300 GHz. In the 1960s, researchers used microwave sintering for the first time in the preparation of ceramic materials, and in the mid-1970s the microwave sintering technology was studied in a more comprehensive and systematic way. In the late 1980s, microwave sintering technology was frequently applied to cermet materials with excellent properties [226]. Compared with hot press sintering, microwave sintering has many features and advantages: (1) The thermal effect of microwaves is mainly provided by the conductivity losses and dielectric losses caused by the electric field part and the magnetic losses caused by the magnetic field part [227]. The sintered material itself becomes a heat source, generating heat inside the material and transferring it outward. For microwave sintering technology, due to the method of heat transfer from the inside to the outside, a negative temperature gradient is created inside the sample and ultimately the holistic heating of the specimen is realized [228]. Compared with the traditional sintering method, it can effectively reduce the heat loss in the heating process, improve the energy utilization, avoid the phenomenon of high temperature on the sample surface and low temperature inside the sample caused by the traditional heating, meanwhile reduce the deformation and cracking phenomenon of the sample caused by thermal stress. During the sintering process with different substances, the monolithic sintering characteristics can effectively reduce the generation of internal stresses, provide a larger driving force for the ceramic billet, and significantly increase the density of the material. At the same time, due to the higher heating rate of microwave sintering technology, the sintering cycle has also been greatly reduced, limiting the grain size, which is conducive to the preparation of high-density ceramic materials [229]; (2) The coupling effect between microwaves and various types of materials is related to their microwave

properties, including the electrical conductivity, magnetic permeability and dielectric constant of the material [230]. The different dielectric properties of the material, and the microwave coupling effect are different [231]. In the non-homogeneous system of materials for the heating process, the electromagnetic field is preferentially coupled with high-loss materials, and then coupled with low dielectric loss materials, and therefore can be adjusted through the distribution of the electromagnetic field or the composition of the material to control the heating process, to produce ceramic materials with a special structure or special properties [232]. For example, adding some SiC particles to  $\text{Al}_2\text{O}_3$  powder particles, during the microwave sintering process, the microwave preferentially reacts with the SiC particles, which have a stronger absorption capacity at room temperature, in a coupling reaction, and subsequently transfers the heat to the  $\text{Al}_2\text{O}_3$  powder particles, to rapidly heat the particles to achieve the purpose of preheating. When the  $\text{Al}_2\text{O}_3$  powder particles reach the critical temperature, their dielectric loss increases significantly, and they begin to be coupled with microwave heating. The disadvantage of selective microwave heating is that it can cause thermal focusing inside the specimen, leading to thermal runaway phenomenon, which requires special attention when selective microwave sintering of multi-component materials [233]; (3) Microwave coupling with different substances will appear to accelerate the atomic movement, reduce the sintering temperature, enhance the heating rate, affect the crystalline phase transition, the rapid formation of the sintering neck, and other special phenomena can be summarized as "non-thermal effects" [234]. The research on non-thermal effects of different substances has become the focus of current research, but due to the current lack of characterization means, the mechanism of non-thermal effects is only limited to the initial exploration stage.

Since the heating method of microwave sintering technology is different from the traditional heat transfer and radiant heat transfer of hot press sintering, it is necessary to select suitable materials according to the heating principle before using microwave sintering. Due to the different materials have different dielectric loss abilities and microwave responsive abilities, so according to this characteristic can be distinguished into microwave absorbing materials, microwave reflective materials, and microwave transparent materials [235]. The stronger the dielectric loss capability of the material, the stronger its coupled thermal and plasma effects with microwave excitation, and the easier it is to sinter materials with new microstructures and excellent properties under the combination of the two thermal effects.

Fig. 15 shows a schematic diagram of a microwave sintering furnace commonly used in industry, including an insulation box, a microwave generator, a SiC susceptor, a control system, and a thermocouple [236]. The microwave generated by the microwave generator

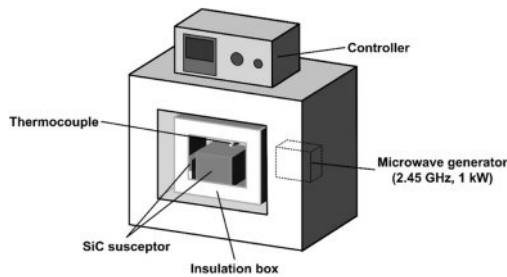


Fig. 15. Schematic of the microwave sintering furnace [236].

is transferred to the SiC susceptor and coupled with the material inside the insulation box for heating, and the equipment can be applied to the microwave sintering of most ceramic materials.

Song et al. [237] prepared (MgCoNiCuZn)O high-entropy ceramics using microwave sintering technology and investigated the effect of sintering temperature on the microstructure of the ceramics. The results showed that the single-phase (MgCoNiCuZn)O high-entropy ceramics could be prepared in about 1 h when the preform pressure was 5 MPa and the temperature was higher than 900 °C, and the density of the samples increased gradually with the increase of temperature. When the temperature was higher than 1000 °C, the pores in the samples indicated that the Cu atoms accumulated, agglomerated, and polarized at the grain boundaries.

### Ultrafast high-temperature sintering

In 2020, Wang et al. [238] first reported the ultrafast high-temperature sintering (UHS) technology, and the core principle of this technology is to realize rapid heating-holding-cooling by high-power radiation in an inert atmosphere. Ultimately, the rapid and efficient sintering of materials is accomplished, which is a highly universal sintering process. The principle of UHS is shown in Fig. 16 [239]. The carbon felt and carbon paper generate a large amount of Joule heat under the action of electric current, so that the whole sintering system can reach a high temperature (up to 3000 °C under an inert gas environment) in a short time and realize rapid

sintering of ceramic green bodies through radiation and heat conduction. Compared with the traditional hot press sintering method, UHS has the characteristics of uniform temperature distribution, fast heating/cooling speed, and high sintering temperature. The shortest sintering process can be shortened to 10 s, and the efficiency is much higher than the traditional hot press sintering process [240].

Ultrafast high-temperature sintering technology has been applied to the research of rapid densification of high-entropy ceramics. Spiridigliozzis et al. [241] successfully prepared high-entropy fluorite oxide ceramics  $Ce_{0.2}Zr_{0.2}Y_{0.2}Gd_{0.2}La_{0.2}O_{2-\delta}$  by UHS technique and investigated the effects of current and sintering time on high-entropy ceramics. The results showed that when the current was 20 A, the samples were hardly sintered and the relative density was only 70%; when the maximum current was 25 A, ceramic blocks with high relative density could be obtained regardless of the sintering time (10 s, 20 s, and 60 s). In addition, they compared with the samples sintered by the traditional solid-state sintering, and found that the grains of the UHS samples were finer, with an average grain size of only 347 nm, and the samples obtained by the solid-state method had more serious grain coarsening, with an average grain size of 10  $\mu\text{m}$ .

Ye et al. [242] prepared  $(La_{0.2}Nd_{0.2}Sm_{0.2}Eu_{0.2}Gd_{0.2})_2Hf_2O_7$  ceramics by UHS technique and characterized their hardness and high-temperature stability. They homogeneously mixed the original oxide powders and pressed them into circular green bodies, which were later placed in the middle of a carbon felt. To uniformly distribute the heat in the samples, the heating program was set as a staged heating, with the current reaching 20 A, 30 A, 40 A, and 50 A for 20 s, 20 s, 20 s, and 150 s, respectively. The final high-entropy ceramics were prepared with a micro-hardness of 1089  $HV_{0.3}$  and very low thermal conductivity ( $0.93 \text{ W}\cdot\text{m}^{-1}\cdot\text{K}^{-1}$ ). On this basis, Ye et al. [243] prepared defective fluorite high-entropy ceramics  $(Y_{0.2}Dy_{0.2}Er_{0.2}Tm_{0.2}Yb_{0.2})_4Hf_3O_{12}$  by a step-up heating method, and the samples were sintered at a current of 52 A for 150 s. The final high-entropy ceramics obtained had a high coefficient of thermal

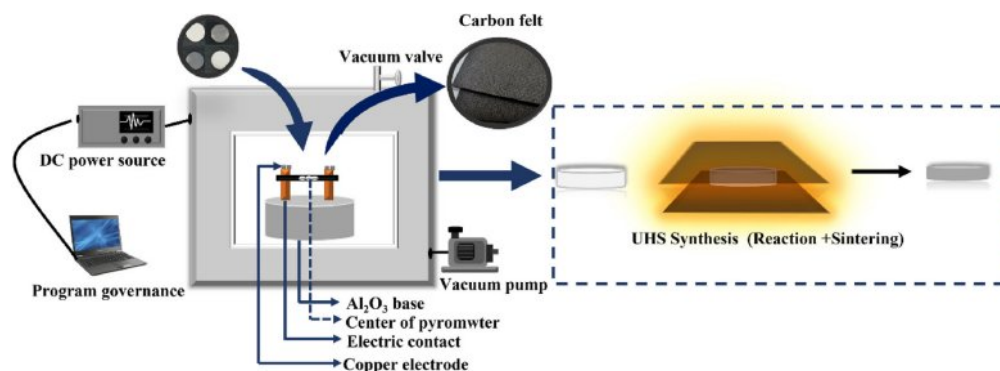


Fig. 16. Schematic illustration of the UHS apparatus [239].

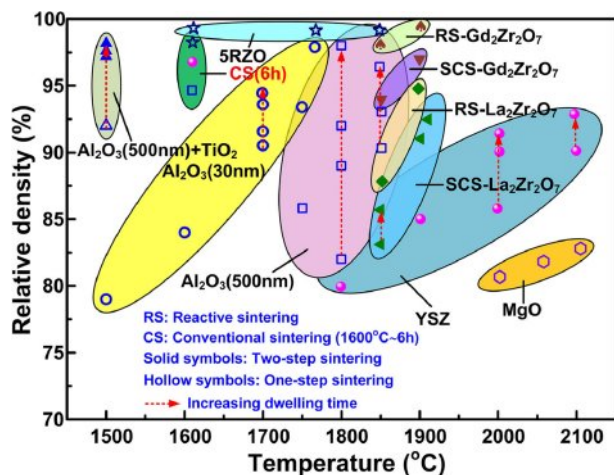


Fig. 17. Relative density versus temperature for a variety of ceramics prepared by UHS (dwelling time  $\leq 30$  s; heating and cooling rates: 500–1000  $^{\circ}\text{C}/\text{min}$ , depending on the thermal conductivity of ceramics) [244].

expansion ( $11.23 \times 10^{-6} \text{ K}^{-1}$ ), low thermal conductivity ( $0.94 \text{ W} \cdot \text{m}^{-1} \cdot \text{K}^{-1}$ , 1300  $^{\circ}\text{C}$ ), and a low grain growth rate ( $0.088\text{--}0.096 \mu\text{m} \cdot \text{h}^{-1}$ , 1500  $^{\circ}\text{C}$ ).

Guo et al. [244] prepared three oxide ceramics,  $\text{Al}_2\text{O}_3$ ,  $\text{La}_2\text{Zr}_2\text{O}_7$ , and  $(\text{La}_{0.2}\text{Nd}_{0.2}\text{Sm}_{0.2}\text{Eu}_{0.2}\text{Gd}_{0.2})_2\text{Zr}_2\text{O}_7$ , by UHS technique (Fig. 17). The high-entropy powders were synthesized by solution combustion method and then pressed into blanks and subjected to ultrafast high-temperature sintering at 1600  $^{\circ}\text{C}$  for 30 s. The relative density of the final samples was about 99%. In contrast, the relative density of the solid-state sintering sample obtained by pressureless sintering at the same temperature for 6 h was only 95%, which was lower than that of the UHS sample. To investigate the mechanism of the electrical and thermal effects on the rapid densification during the sintering process of UHS, they prepared  $(\text{La}_{0.2}\text{Nd}_{0.2}\text{Sm}_{0.2}\text{Eu}_{0.2}\text{Gd}_{0.2})_2\text{Zr}_2\text{O}_7$  coated with BN nanopowder on the surface using the same sintering process, and the samples also had very high relative densities (99%), which proved that the thermal effect plays a dominant role in the process of rapid densification. However, the high entropy ceramic sintered bodies isolated from electrical effects differ from pure  $(\text{La}_{0.2}\text{Nd}_{0.2}\text{Sm}_{0.2}\text{Eu}_{0.2}\text{Gd}_{0.2})_2\text{Zr}_2\text{O}_7$  in fracture morphology, with the former fracturing along the grain and the latter through the grain with higher grain boundary strength, which proved that the electrical effect is favorable to increase the grain boundary strength of sintered blocks.

Xie et al. [245] combined UHS with liquid phase-assisted sintering to prepare high-entropy boride ceramics. A mixture of  $(\text{Ti}_{0.2}\text{Ta}_{0.2}\text{Mo}_{0.2}\text{W}_{0.2}\text{Zr}_{0.2})\text{B}_2$  and  $\text{B}_4\text{C}$  was rapidly heated up to 3000 K and held for 2 min, and it was found that a eutectic liquid was formed at the interface between high-entropy ceramics and boron carbide, and this eutectic liquid was able to fill the intergranular gaps and form  $\text{ZrB}_{12}$  distributed along the

crystals. When the sintering temperature was 2400 K, the sintering driving force of surface energy reduction was very small, the sintered bodies contained more pores, and only a small amount of eutectic liquid formation, so it was necessary to extend the heat treatment time to complete the densification; When the sintering temperature was 3000 K, the  $(\text{Ti}_{0.2}\text{Ta}_{0.2}\text{Mo}_{0.2}\text{W}_{0.2}\text{Zr}_{0.2})\text{B}_2$  still remained solid-state, the amount of eutectic liquid generation was moderate, and the samples were able to complete the sintering within a short time; When the sintering temperature rose to 3300 K, the  $(\text{Ti}_{0.2}\text{Ta}_{0.2}\text{Mo}_{0.2}\text{W}_{0.2}\text{Zr}_{0.2})\text{B}_2$  ceramic started to melt, and the sample could not maintain its original state. In summary, 3000 K was a more suitable temperature, and the high-entropy boride composites prepared by UHS had high hardness, with a Vickers hardness of 36.4 GPa (load 0.49 N), which was much higher than that of the pure high-entropy boride without  $\text{B}_4\text{C}$  and  $\text{ZrB}_{12}$ . It was demonstrated that the liquid phase-assisted ultrahigh-temperature sintering technique contributed to the densification of the composites.

## Conclusion and Prospect

As a novel ceramic material system, high-entropy ceramics are characterized by a complex composition, a large research system, a unique entropy effect, and modifiable material properties. This paper describes and analyzes the research progress of the application of advanced synthesis and sintering technologies in the preparation of high-entropy ceramics. In the process of synthesizing high-entropy ceramic powders, factors such as synthesis process, material composition, particle size distribution, and type of additives need to be considered. The production of high-quality ceramic powder needs to be through strict process control and raw material selection, for any structure and composition of ceramic powder, the preparation process is the basis of ceramic performance, the performance of the final ceramic product has a decisive impact, and high-performance ceramic powders and slurries prepared with the upgrading of process equipment is inseparable. At present, high-performance high-entropy ceramics require the raw powder with high purity, fine particle size, narrow particle size distribution, and stable properties. Among the existing industrialized production processes, ball milling and solid-state reaction methods are characterized by abundant raw materials and simple processes, but the main drawbacks of the two methods are incomplete conversion of raw materials, large powder particle size, and wide distribution. Therefore, the development of new powder synthesis technology to shorten the process flow, improve the feasibility of industrialized production and obtain ideal powder samples has become the development goal of high-entropy ceramic powder synthesis technology. In the sintering of high-entropy ceramics, the traditional sintering technology has the disadvantages of long

sintering time, high sintering temperature, difficulty in making high-entropy ceramics dense, and coarse grains of sintered samples, which hinder the application and research of high-entropy ceramic materials. Therefore, the development of new sintering technology to shorten the sintering time, reduce the sintering temperature, and optimize the thermomechanical properties of the sintered samples has become the development goal of high-entropy ceramic sintering technology. It has been shown that advanced sintering technology is an important way to obtain high-entropy ceramics with excellent properties. Among them, advanced sintering technologies such as spark plasma sintering, flash sintering, and ultrafast high-temperature sintering have great potential in the preparation of high-entropy ceramics and have obvious advantages in enhancing the properties of high-entropy ceramics such as relative density, fracture toughness and hardness. Although the powder synthesis and the sintering technology of high-entropy ceramics have made certain research progress, the relevant direction is still worthy of in-depth exploration, which can be considered from the following aspects:

The current research and development of high-entropy ceramics has been from the original tendency to single-phase and high-purity features to the direction of multi-phase composite development, the main purpose of the composite is to give full play to the ceramic material's high hardness, high temperature, corrosion resistance, and improve the toughness. Among them, the multi-phase toughened high-entropy ceramic is achieved by introducing a second-phase ceramic with ferroelasticity into the original ceramic phase. When the introduced second-phase material has a high Curie temperature, the toughening of high-entropy ceramics can be realized at high temperatures. Therefore, it is crucial to study the synthesis process of complex-phase high-entropy ceramic powders to explore the distribution behavior of different phases as well as the toughening mode.

Combining a single new sintering technology with other sintering technologies, such as through the two-step sintering method to obtain a dense block at the same time can effectively inhibit grain coarsening and improve the mechanical properties of the sample. Currently, there are relevant studies on two-step spark plasma sintering and two-step flash sintering. Combining two-step sintering with new sintering technology not only retains the advantages of new sintering technology such as high efficiency and low energy consumption, but also can realize grain refinement and further improve the performance of ceramic materials. In the future, the research and application of sintering technology should pay attention to the combination of multiple sintering technologies, give full play to the advantages of traditional sintering technology and advanced sintering technology, and promote the research and development of materials.

Development of nanoscale high-entropy ceramic

powders with grain size, grain boundary width, second-phase distribution, pore size, and defect size controlled on the nanometer scale. Due to the grain refinement contributes to the inter-grain slip and makes the ceramics superplastic, so the grain refinement can improve the original properties of ceramics. The development of nanoceramics is an important trend in the current ceramic research and development, which will prompt the research of ceramic materials from process to theory, from performance to application are upgrade to a new stage.

## Acknowledgement

This work is supported by the National Natural Science Foundation of China (51702145), Liaoning Provincial Department of Education Project Services Local Project (FWDF202003).

## Declarations

**Conflict of interest** The authors declare that they have no known competing financial interests or personal relationships that could have appeared to influence the work reported in this paper.

## References

1. J.W. Sun, X.Y. Wan, T. Yang, D.Y. Ma, and J.M. Wang, *J. Inorg. Mater.* 38[12] (2023) 1434-1440.
2. J.H. Liu, Y.Y. Wang, Z. Lu, Y.G. Jung, G.L. Lyu, Y.W. Zhou, J. Zhang, and Y. Li, *J. Ceram. Process. Res.* 25[5] (2024) 875-903.
3. J.W. Yeh, S.K. Chen, J.Y. Gan, S.J. Lin, T.S. Chin, T.T. Shun, C.H. Tsau, and S.Y. Chang, *Metall. Mater. Trans. A* 35A (2004) 2533-2536.
4. J.W. Yeh, S.K. Chen, S.J. Lin, J.Y. Gan, T.S. Chin, T.T. Shun, C.H. Tsau, and S.Y. Chang, *Adv. Eng. Mater.* 6[5] (2004) 299-303.
5. H. Zhao, Z. Zheng, H.R. Zhou, L. Chang, K. Tsoutas, L.M. Yang, S.K. Alavi, Y.P. Liu, B. Akhavan, M.M. Bilek, and Z.W. Liu, *Surf. Interfaces* 37 (2023) 102692.
6. J. Zhu, X. Meng, J. Xu, P. Zhang, Z. Lou, M.J. Reece, and F. Gao, *J. Eur. Ceram. Soc.* 41[1] (2021) 1052-1057.
7. C. Zhang, J.K. Zhu, G.Q. Zhang, and Y.W. Hu, *J. Alloys Compd.* 927 (2022) 167110.
8. K. Yuan, T.Z. Tu, C. Shen, L. Zhou, J.X. Liu, J. Li, K.Y. Xie, and G.J. Zhang, *J. Adv. Ceram.* 11 (2022) 882-892.
9. B. Cantor, *Ann. Chem.-Sci. Mater.* 32[3] (2007) 245-256.
10. J. Li, Q.H. Fang, and P.K. Liaw, *Adv. Eng. Mater.* 23[1] (2021) 2001044.
11. C.M. Rost, E. Sachet, T. Borman, A. Moballeggh, E.C. Dickey, D. Hou, J.L. Jones, S. Curtarolo, and J.P. Maria, *Nat. Commun.* 6 (2015) 8485.
12. S. Akrami, P. Edalati, M. Fuji, and K. Edalati, *Mater. Sci. Eng. R Rep.* 146 (2021) 100644.
13. W.L. Hsu, C.W. Tsai, A.C. Yeh, and J.W. Yeh, *Nat. Rev. Chem.* 8 (2024) 471-485.
14. S.J. McCormack, and A. Navrotsky, *Acta Mater.* 202 (2021) 1-21.
15. A. Sarkar, Q.S. Wang, A. Schiele, M.R. Chellali, S.S.



- Bhattacharya, D. Wang, T. Brezesinski, H. Hahn, L. Velasco, and B. Breitung, *Adv. Mater.* 31[26] (2019) 1806236.
16. X.T. Li, A.G. Sheinerman, H. Yang, and Z.Y. Zhu, *Int. J. Plast.* 154 (2022) 103304.
17. Y.Z. Li, and Y. Shi, *Opt. Laser Technol.* 134 (2021) 106632.
18. I. Moravcik, J. Cizek, J. Zapletal, Z. Kovacova, J. Vesely, P. Minarik, M. Kitzmantel, E. Neubauer, and I. Dlouhy, *Mater. Des.* 119 (2017) 141-150.
19. J. Chen, X.Y. Zhou, W.L. Wang, B. Liu, Y.K. Lv, W. Yang, D.P. Xu, and Y. Liu, *J. Alloys Compd.* 760 (2018) 15-30.
20. Y.T. Pan, J.X. Liu, T.Z. Tu, W.Z. Wang, and G.J. Zhang, *Chem. Eng. J.* 451[2] (2023) 138659.
21. G.J. Chen, C.W. Li, H. Li, L. Wang, K.P. Chen, and L.A. An, *J. Eur. Ceram. Soc.* 41[16] (2021) 309-314.
22. W. Li, Y.A. Sun, L. Ye, W.J. Han, F.H. Chen, J.L. Zhang, and T. Zhao, *J. Am. Ceram. Soc.* 105[6] (2022) 3729-3734.
23. B. Du, H.H. Liu, and Y.H. Chu, *J. Am. Ceram. Soc.* 103[8] (2020) 4063-4068.
24. Y. Zhang, W.M. Guo, Z.B. Jiang, Q.Q. Zhu, S.K. Sun, Y. You, K. Plucknett, and H.T. Lin, *Scr. Mater.* 164 (2019) 135-139.
25. Y. Qin, J.C. Wang, J.X. Liu, X.F. Wei, F. Li, G.J. Zhang, C.X. Jing, J.W. Zhao, and H.Z. Wu, *J. Eur. Ceram. Soc.* 40[8] (2020) 2752-2759.
26. X.Q. Chen, and Y.Q. Wu, *J. Am. Ceram. Soc.* 103[2] (2020) 750-756.
27. Z.F. Zhao, H.M. Xiang, F.Z. Dai, Z.J. Peng, and Y.C. Zhou, *J. Mater. Sci. Technol.* 35[10] (2019) 2227-2231.
28. B. Zhao, Z.K. Yan, D.P. Li, X.D. Zhou, Y.Q. Du, Y.Y. Wu, L.T. Yang, J.C. Zhang, D.W. Zhang, and R.C. Che, *ACS Appl. Mater. Interfaces* 15[51] (2024) 59618-59629.
29. A.O. Moghaddam, and E.A. Trofimov, *J. Alloys Compd.* 851 (2021) 156838.
30. M. Guo, F.N. Zhang, Y. Miao, Y.F. Liu, J. Yu, and F. Gao, *J. Inorg. Mater.* 36[4] (2021) 431-435.
31. W.C. Hong, F. Chen, Q. Shen, Y.H. Han, W.G. Fahrenholtz, and L.M. Zhang, *J. Am. Ceram. Soc.* 102[4] (2019) 2228-2237.
32. Z. Teng, Y.Q. Tan, and H.B. Zhang, *Materials* 15[1] (2022) 129.
33. B. Wang, J.C. Yao, J.H. Wang, and A.M. Chang, *J. Alloys Compd.* 897 (2022) 163188.
34. Z. Teng, Y.Q. Tan, S.F. Zeng, Y. Meng, C. Chen, X.C. Han, and H.B. Zhang, *J. Eur. Ceram. Soc.* 41[6] (2021) 3614-3620.
35. L. Xiao, L.W. Deng, Y.X. Li, Z.J. Qing, Y.C. Xi, J.H. Zhu, and S. Peng, *J. Eur. Ceram. Soc.* 44[1] (2024) 277-283.
36. J.J. He, G. He, J. Liu, and J.C. Tao, *J. Eur. Ceram. Soc.* 41[12] (2021) 6080-6086.
37. M.T. Duan, I.V. Solodkiy, and Y.I. Bogomol, *J. Superhard Mater.* 45 (2024) 434-443.
38. D. Moskovskikh, S. Vorotilo, V. Buinevich, A. Sedegov, K. Kuskov, A. Khort, C. Shuck, M. Zhukovskiy, and A. Mukasyan, *Sci. Rep.* 10 (2020) 19874.
39. W.Y. Yang, Z. Han, and G.P. Zheng, *Scr. Mater.* 203 (2021) 114096.
40. L. Shao, H.H. Jiang, C.R. Xu, N. Ding, and B.Y. Tang, *J. Alloys Compd.* 954 (2023) 170205.
41. B.H. Zhang, Y.W. Wang, J. Yin, Y.C. Wang, H.F. Zhang, T. Csanadi, J. Dusza, M.J. Reece, N. Lin, X. Yang, X.J. Liu, Z.R. Huang, and D.L. Jiang, *J. Mater. Sci. Technol.* 164 (2023) 205-214.
42. D. Bérardan, S. Franger, D. Dragoe, A.K. Meena, and N. Dragoe, *Phys. Status Solidi RRL* 10[4] (2016) 328-333.
43. Y.X. Li, Y.M. Lei, S. Zhao, H. Xiao, H.C. Liu, Y.G. Wang, Y.X. Luo, J. Zhang, J.Y. Wang, R.C. Ewing, and C.X. Wang, *Scr. Mater.* 229 (2023) 115367.
44. J.X. Wu, M. Zhang, Z.Q. Li, M.Z. Huang, H.M. Xiang, L.Y. Xue, Z.M. Jiang, Z.G. Zhao, L.F. Wei, Y. Zheng, F. Yang, G. Ran, Y.C. Zhou, and H. Chen, *J. Mater. Sci. Technol.* 155 (2023) 1-9.
45. H.M. Yang, L.X. He, Z.M. Yang, Q.C. Chen, G.Q. Jiang, J.C. Zhu, R. Xue, N. Qiu, and Y. Wang, *J. Alloys Compd.* 968 (2023) 172135.
46. X.Y. Sun, X.H. Zeng, X. He, W. Fang, X. Du, W.X. Li, L. Zhao, and H. Chen, *J. Alloys Compd.* 925 (2022) 166560.
47. R.X. Liu, W.P. Liang, Q. Miao, H. Zhao, S. Ramakrishna, B. Ramasubramanian, X.F. Zhang, Y.D. Song, X.G. Gao, J.K. Du, and X.M. Tao, *J. Mater. Res. Technol.* 27 (2023) 1365-1380.
48. E. Lewin, *J. Appl. Phys.* 127[16] (2020) 160901.
49. S.Y. Hsu, Y.T. Lai, S.Y. Chang, S.Y. Tsai, and J.G. Duh, *Surf. Coat. Technol.* 442 (2022) 128564.
50. S. Jiang, L. Shao, T.W. Fan, J.M. Duan, X.T. Chen, and B.Y. Tang, *Ceram. Int.* 46[10] (2020) 15104-15112.
51. J. Gild, Y. Zhang, T. Harrington, S. Jiang, T. Hu, M.C. Quinn, W.M. Mellor, N. Zhou, K. Vecchio, and J. Luo, *Sci. Rep.* 6 (2016) 37946.
52. L. Feng, W.G. Fahrenholtz, G.E. Hilmas, and F. Monteverde, *J. Eur. Ceram. Soc.* 41[1] (2021) 92-100.
53. J. Gild, J. Braun, K. Kaufmann, E. Marin, T. Harrington, P. Hopkins, K. Vecchio, and J. Luo, *J. Mater. Sci.* 53[3] (2019) 337-343.
54. T. Wang, H. Chen, Z.Z. Yang, J.Y. Liang, and S. Dai, *J. Am. Chem. Soc.* 142[10] (2020) 4550-4554.
55. Z.F. Zhao, H. Chen, H.M. Xiang, F.Z. Dai, X.H. Wan, Z.J. Peng, and Y.C. Zhou, *J. Mater. Sci. Technol.* 35[12] (2019) 2892-2896.
56. N. Kamaya, K. Homma, Y. Yamakawa, M. Hirayama, R. Kanno, M. Yonemura, T. Kamiyama, Y. Kato, S. Hama, K. Kawamoto, and A. Mitsui, *Nat. Mater.* 10 (2011) 682-686.
57. T.X. Nguyen, Y.H. Su, C.C. Lin, and J.M. Ting, *Adv. Funct. Mater.* 31[48] (2021) 2106229.
58. G.R. Zhang, Y.Q. Wu, *Int. J. Appl. Ceram. Technol.* 19[2] (2022) 644-672.
59. S. Schweidler, Y.S. Tang, L. Lin, G. Karkera, A. Alsawaf, L. Bernadet, B. Breitung, H. Hahn, M. Fichtner, A. Tarancon, and M. Botros, *Front. Energy Res.* 10 (2022) 983979.
60. X. Liu, *Int. J. Nanotechnol.* 18[1-4] (2021) 214-225.
61. C.S. Lu and F. Ye, *Acta Metall. Sin.* 53[1] (2017) 10-18.
62. Z. Teng, L.N. Zhu, Y.Q. Tan, S.F. Zeng, Y.H. Xia, Y.G. Wang, and H.B. Zhang, *J. Eur. Ceram. Soc.* 40[4] (2020) 1639-1643.
63. H. Chen, H.M. Xiang, F.Z. Dai, J.C. Liu, and Y.C. Zhou, *J. Mater. Sci. Technol.* 36 (2019) 134-139.
64. J. Gild, M. Samiee, J.L. Braun, T. Harrington, H. Vega, P.E. Hopkins, K. Vecchio, and J. Luo, *J. Eur. Ceram. Soc.* 38[10] (2018) 3578-3584.
65. D.O. Moskovskikh, S. Vorotilo, A.S. Sedegov, K.V. Kuskov, K.V. Bardasova, P.V. Kiryukhantsev-korneev, M. Zhukovskiy, and A.S. Mukasyan, *Ceram. Int.* 46[11] (2020) 19008-19014.
66. E. Chicardi, C. García-Garrido, J. Hernández-Saz, and F.J.

- Gotor, *Ceram. Int.* 46[13] (2020) 21421-21430.
67. Q.S. Peng, W. Jiang, G. Wang, and J.F. Li, *J. Inorg. Mater.* 19 (2004) 1199-1202.
  68. A. Chatterjee, D. Ganguly, R. Sundara, and S.S. Bhattacharya, *Energy Technol.* 12[1] (2024) 2300576.
  69. X.Z. Cao, X.X. Xue, H. Yang, H.T. Li, H.Y. Wang, and L.H. Shi, *Rare Met. Mater. Eng.* 43[8] (2014) 1987-1990.
  70. H. Takizawa, *J. Ceram. Soc. Jpn.* 126[6] (2018) 424-433.
  71. Y.A. Nikiforov, V.A. Danilovsky, V.V. Lozanov, and N.I. Baklanova, *J. Am. Ceram. Soc.* 107[5] (2024) 3587-3599.
  72. J.T. Zhu, Z.H. Lou, P. Zhang, J. Zhao, X.Y. Meng, J. Xu, and F. Gao, *J. Inorg. Mater.* 36[4] (2021) 411-417.
  73. F. Li, L. Zhou, J.X. Liu, Y.C. Liang, and G.J. Zhang, *J. Adv. Ceram.* 8 (2019) 576-582.
  74. X.Y. Meng, J. Xu, J.T. Zhu, P. Zhang, A. Rydosz, M.J. Reece, and F. Gao, *Scr. Mater.* 194 (2021) 113714.
  75. W. Fan, Y. Bai, Y.F. Liu, T.T. Li, B.M. Li, L. Zhang, C.M. Gao, S.Y. Shan, and H.C. Han, *J. Mater. Sci. Technol.* 107 (2022) 149-154.
  76. H.B. Yang, G.Q. Lin, H.P. Bu, H.J. Liu, L.X. Yang, W.J. Wang, X.H. Lin, C. Fu, Y.S. Wang, and C.L. Zeng, *Ceram. Int.* 48[5] (2022) 6956-6965.
  77. T.T. Huang, Y.F. Liu, W. Fan, X.B. Zhong, R. Zou, F. Li, T. Song, T.X. Su, and Y. Bai, *J. Alloys Compd.* 1007 (2024) 176425.
  78. J.T. Zhu, X.Y. Meng, P. Zhang, Z.L. Li, J. Xu, M.J. Reece, and F. Gao, *J. Eur. Ceram. Soc.* 41[4] (2021) 2861-2869.
  79. R. Li, L. He, N. Lin, Y. Niu, A. Li, Z. Wu, Z.Y. Wang, and C. Ma, *J. Eur. Ceram. Soc.* 43[16] (2023) 7273-7281.
  80. Y. Zhang, S.K. Sun, W.M. Guo, L. Xu, W. Zhang, and H.T. Lin, *J. Adv. Ceram.* 10 (2021) 173-180.
  81. J. Gild, A. Wright, K. Quiambao-Tomko, M.D. Qin, J.A. Tomko, M.S. bin Hoque, J.L. Braun, B. Bloomfield, D. Martinez, T. Harrington, K. Vecchio, P.E. Hopkins, and J. Luo, *Ceram. Int.* 46[5] (2020) 6906-6913.
  82. Y. Zhang, S.K. Sun, W. Zhang, Y. You, W.M. Guo, Z.W. Chen, J.H. Yuan, and H.T. Lin, *Ceram. Int.* 46[9] (2020) 14299-14303.
  83. D. Liu, T.Q. Wen, B.L. Ye, and Y.H. Chu, *Scr. Mater.* 167 (2019) 110-114.
  84. L. Feng, W.G. Fahrenholtz, G.E. Hilmas, and Y. Zhou, *Scr. Mater.* 162 (2019) 90-93.
  85. H. Chen, H.M. Xiang, F.Z. Dai, J.C. Liu, and Y.C. Zhou, *J. Mater. Sci. Technol.* 35[10] (2019) 2404-2408.
  86. K.H. Wu, Y. Jiang, S.Q. Jiao, K.C. Chou, and G.H. Zhang, *J. Mater. Res. Technol.* 9[5] (2020) 11778-11790.
  87. K.H. Wu, Y. Wang, K.C. Chou, and G.H. Zhang, *Int. J. Refract. Met. Hard Mater.* 98 (2021) 105567.
  88. Y. Liang, J. Yang, L. Xi, C. Liu, G. Zhang, and W. Zhang, *Mater. Today Phys.* 7 (2018) 54-60.
  89. A.G. Merzhanov and I.P. Borovinskaya, *Combust. Sci. Technol.* 10[5-6] (1975) 195-201.
  90. T. Chanadee, *J. Ceram. Process. Res.* 18[5] (2017) 389-393.
  91. V.D. Valikhov, I.A. Zhukov, D.A. Tkachev, M. Grigoriev, A.E. Matveev, and A.A. Volinsky, *Ceram. Int.* 50[7] (2024) 10974-10981.
  92. D.V. Wagner, V.A. Zhuravlev, K.V. Kareva, R.V. Minin, K.I. Baskakova, O.A. Dotsenko, and A.S. Suraev, *J. Alloys Compd.* 977 (2024) 173437.
  93. E.A. Levashov, A.S. Mukasyan, A.S. Rogachev, and D.V. Shtansky, *Int. Mater. Rev.* 62[4] (2017) 203-239.
  94. T. Kim and M.S. Wooldridge, *J. Am. Ceram. Soc.* 84[5] (2001) 976-982.
  95. S. W. Wang, L. Xiao, Y.B. Hu, G.P. Zhang, H.X. Gao, F.Q. Zhao, G.Z. Hao, and W. Jiang, *Chin. J. Explos. Propellants* 44[6] (2021) 705-734.
  96. B.L. Zuo, P.J. Liu, W.H. Zhang, and Q.L. Yan, *Chin. J. Energ. Mater.* 26[6] (2018) 537-544.
  97. Z.N. Li, P.Q. La, Q. Meng, H.D. Wang, W.K. Wang, J.L. Kang, and Y.L. Pu, *Mater. Rep.* 37[19] (2023) 70-77.
  98. P. Mossino, *Ceram. Int.* 30[3] (2004) 311-332.
  99. Y.X. Chen, J.T. Li, and J.S. Du, *Mater. Res. Bull.* 43[6] (2008) 1598-1606.
  100. C. Milanese, F. Maglia, A. Tacca, U. Anselmi-Tamburini, C. Zanotti, and P. Giuliani, *J. Alloys Compd.* 421[1-2] (2006) 156-162.
  101. R. Fu, K. Chen, S. Agathopoulos, and J.M.F. Ferreira, *J. Cryst. Growth* 296[1] (2006) 97-103.
  102. E. Nikolay, M. Alexey, B. Ivan, and Z. Ilya, *Mater. Lett.* 346 (2023) 134562.
  103. G. Tallarita, R. Licheri, S. Garroni, R. Orrù, and G. Cao, *Scr. Mater.* 158 (2019) 100-104.
  104. X.W. Luo, S. Huang, C.H. Xu, S.E. Hou, and H.Y. Jin, *Ceram. Int.* 49[1] (2023) 766-772.
  105. N.S. Evseev, A.E. Matveev, P.Y. Nikitin, Y.A. Abzaev, and I.A. Zhukov, *Ceram. Int.* 48[11] (2022) 16010-16014.
  106. E. Pakhomova, G.C.M. Gao, R. Orrù, S. Garroni, P. Ferro, and R. Licheri, *Materials* 17[3] (2024) 718.
  107. A. Ghanbari, M. Sakaki, A. Faeghinia, M.S. Bafghi, and K. Yanagisawa, *Bull. Mater. Sci.* 39 (2016) 925-933.
  108. M.A. Korchagin, A.I. Gavrilov, I.V. Grishina, D.V. Dudina, A.V. Ukhina, B.B. Bokhonov, and N.Z. Lyakhov, *Combust., Explos. Shock Waves* 58 (2022) 46-53.
  109. E.A. Juarez-Arellano, A. Martinez-Garcia, B. Winkler, T. Pérez-López, and J.M. Padilla, *Ceram. Int.* 49[2] (2022) 2350-2358.
  110. F. Kaya, K.C. Dizdar, S. Aliakbarlu, G.I. Selimoglu, and B. Derin, *Mater. Chem. Phys.* 318 (2024) 129304.
  111. S. Sakka, *J. Sol-Gel Sci. Technol.* 102 (2022) 478-481.
  112. A. Cestari, L.R. Avila, E.C.O. Nassor, P.F.D. Pereira, P.S. Calefi, K.J. Ciuffi, S. Nakagaki, A.C.P. Gomes, and E.J. Nassar, *Mater. Res.* 12[2] (2009) 139-143.
  113. J. Guo and W. Li, *ACS Appl. Energy Mater.* 5[1] (2022) 397-406.
  114. L. Gao, Y. Zhang, X. Yang, Y.B. He, and L.H. Song, *J. Ceram. Process. Res.* 21[6] (2020) 615-621.
  115. M.M. Wang, R.M. Wang, H.Y. Dai, T. Li, Y. Sun, D.W. Liu, F.F. Yan, and T.D. Ping, *Ceram. Int.* 48[15] (2022) 21622-21630.
  116. S. Didde and R.S. Dubey, *Sci. Rep.* 14 (2024) 13684.
  117. X.S. Zhang, L.Y. Xue, F. Yang, Z.H. Shao, H. Zhang, Z.G. Zhao, and K.X. Wang, *J. Alloys Compd.* 863 (2021) 158763.
  118. D.H. Guo, F.F. Zhou, B.S. Xu, Y.G. Wang, and Y. Wang, *Ceram. Int.* 48[21] (2022) 32532-32535.
  119. Y. Yang, J.Q. Bi, X.C. Gao, K.N. Sun, L.J. Qiao, G.D. Liang, and H.Y. Wang, *Ceram. Int.* 49[11] (2023) 19523-19527.
  120. D.B. Liu, Y.G. Wang, F.F. Zhou, B.S. Xu, and B.W. Lv, *Ceram. Int.* 47[21] (2021) 29960-29968.
  121. Z.H. Zhang, S.Z. Yang, X.B. Hu, H.D. Xu, H.G. Peng, M.M. Liu, B.P. Thapaliya, K.C. Jie, J.H. Zhao, J.X. Liu, H. Chen, Y. Leng, X.Y. Lu, J. Fu, P.F. Zhang, and S. Dai, *Chem. Mater.* 31[15] (2019) 5529-5536.
  122. S.T. Aruna and A.S. Mukasyan, *Curr. Opin. Solid State Mater. Sci.* 12[3-4] (2008) 44-50.
  123. T.M. Vidyuk, M.A. Korchagin, D.V. Dudina, and B.B. Bokhonov, *Combust., Explos. Shock Waves* 57 (2021) 385-397.

124. E. Carlos, R. Martins, E. Fortunato, and R. Branquinho, *Chem. - Eur. J.* 26[42] (2020) 9099-9125.
125. U. Shashikumar, B.C. Jha, S. Chawla, C.M. Hussain, G. Andaluri, Y.C. Lin, and V.K. Ponnusamy, *Fuel* 336 (2023) 126829.
126. C.H. Jung, S. Jalota, and S.B. Bhaduri, *Mater. Lett.* 59[19-20] (2005) 2426-2432.
127. N. Sisakyan, G. Chilingaryan, A. Manukyan, and A.S. Mukasyan, *Nanomaterials* 13[23] (2023) 3030.
128. A.Q. Mao, H.Z. Xiang, Z.G. Zheng, K. Kuramoto, H.Y. Yu, and S.L. Ran, *J. Magn. Magn. Mater.* 484 (2019) 245-252.
129. F.T. Li, J.R. Ran, M. Jaroniec, and S.Z. Qiao, *Nanoscale* 7[42] (2015) 17590-17610.
130. R.K. Tamrakar, D.P. Bisen, K. Upadhyay, M. Sahu, I.P. Sahu, and M. Bramhe, *Superlattices Microstruct.* 88 (2015) 382-388.
131. N. Verma, J. Kaur, V. Dubey, N. Dubey, and T. Ram, *Inorg. Chem. Commun.* 147 (2023) 110234.
132. C.H. Jung, *J. Nucl. Mater.* 341[2-3] (2005) 148-152.
133. L.K. Cong, W. Li, J.C. Wang, S.Y. Gu, and S.Y. Zhang, *J. Mater. Sci. Technol.* 101 (2022) 199-204.
134. C.Y. Zuo, S.L. Yang, Z.Q. Cao, W.J. Jie, and X.H. Wei, *Ceram. Int.* 49[15] (2023) 25486-25494.
135. L.K. Cong, S.Y. Zhang, S.Y. Gu, and W. Li, *J. Mater. Sci. Technol.* 85 (2021) 152-157.
136. A. Gautam and M.I. Ahmad, *Ceram. Int.* 47[15] (2021) 22225-22228.
137. Z.Y. Yin, S. Li, X. Li, W.Y. Shi, W. Liu, Z.X. Gao, M.Y. Tao, C.L. Ma, and Y. Liu, *RSC Adv.* 13[5] (2023) 3265-3277.
138. E. Novitskaya, J.P. Kelly, S. Bhaduri, and O.A. Graeve, *Int. Mater. Rev.* 66[3] (2021) 188-214.
139. J.B. Zhang, L.W. Fan, J.L. Li, X.F. Liu, R.W. Wang, L. Wang, and G.L. Tu, *Nano Res.* 12 (2019) 121-127.
140. M. Malik, K.H. Chan, and G. Azimi, *Mater. Today Energy* 28 (2022) 101066.
141. C. Zhang, H.F. Liu, Z.L. Qie, Z.Y. Hu, J.H. Xie, G.G. Liu, and Y.L. Wang, *Ceram. Int.* 49[22] (2023) 34826-34836.
142. Y.S. Jun, Y.G. Zhu, Y. Wang, D. Ghim, X.H. Wu, D. Kim, and H. Jung, *Annu. Rev. Phys. Chem.* 73 (2022) 453-477.
143. D. Liu, S.M. Gao, Y. Zhang, S.T. Yu, and F. Wang, *Ceram. Int.* 45[17] (2019) 21804-21809.
144. X.W. Luo, S. Huang, R.Q. Huang, S. Hou, and H.Y. Jin, *J. Eur. Ceram. Soc.* 44[4] (2024) 2452-2459.
145. Y. Wen, C.L. Zhou, L.F. Yu, Q. Zhang, W.X. He, and Q.S. Liu, *Solid State Sci.* 142 (2023) 107237.
146. J.J. Du, Y. Sun, J. Zhu, Q. Li, B. Wang, J.T. Liu, and X.R. Meng, *Mater. Rep.* 38[5] (2024) 115-123.
147. P. Prasertdam, M. Inoue, O. Mekasuvandumrong, W. Thanakulrangsarn, and S. Phatanasri, *Inorg. Chem. Commun.* 3[11] (2000) 671-676.
148. K. Ozeki, H. Aoki, and T. Masuzawa, *Appl. Surf. Sci.* 256[23] (2010) 7027-7031.
149. Y.H. Xing, H. Liang, X.L. Li, and L.Q. Si, *Particuology* 7[5] (2009) 414-418.
150. W.Y. Sun, F. Zhang, X. Zhang, T. Shi, J.R. Li, Y. Bai, C. Wang, and Z.J. Wang, *Ceram. Int.* 48[13] (2022) 19492-19500.
151. P.F. Yu, Z.F. Ma, C.Q. Liu, W.F. Liu, S.W. Zhao, Z. Han, T.Q. Shao, P.D. Gao, B.R. Jiang, and X.B. Gu, *Ceram. Int.* 48[11] (2022) 15992-15999.
152. A.B. Workie, H.S. Ningsih, and S.J. Shih, *J. Anal. Appl. Pyrolysis* 170 (2023) 105915.
153. J. Leng, Z.X. Wang, J.X. Wang, H.H. Wu, G.C. Yan, X.H. Li, H.J. Guo, Y. Liu, Q.B. Zhang, and Z.P. Guo, *Chem. Soc. Rev.* 48[11] (2019) 3015-3072.
154. H. Shimada, E. Takami, K. Takizawa, A. Hagiwara, and M. Ihara, *Solid State Ionics*, 193[1] (2011) 43-51.
155. G.L. Messing, S.C. Zhang, and G.V. Jayanthi, *J. Am. Ceram. Soc.* 76[11] (1993) 2707-2726.
156. K.R. Nemade, R.V. Barde, and S.A. Waghuley, *Ceram. Int.* 41[3] (2015) 4836-4840.
157. T. Sasikala, K. Shanmugasundaram, P. Thirunavukkarasu, J. Chandrasekaran, P. Vivek, R. Marnadu, M.A. Manthrammel, and S. Gunasekaran, *Inorg. Chem. Commun.* 130 (2021) 108701.
158. P. Nie, G.Y. Xu, J.M. Jiang, H. Dou, Y.T. Wu, Y.D. Zhang, J. Wang, M.Y. Shi, R.R. Fu, and X.G. Zhang, *Small Methods* 2[2] (2018) 1700272.
159. L. Wang, T.A. Zhang, G.Z. Lv, W.G. Zhang, Y. Liu, Z.H. Dou, and L.P. Niu, *Green Process. Synth.* 7[5] (2018) 464-469.
160. W.P. Zheng, J.J. Wang, P. Liu, X. Ma, K. Zhang, F.C. Ma, and W. Li, *Rare Met. Mater. Eng.* 52[12] (2023) 4284-4294.
161. A. Sarkar, R. Djenadic, D. Wang, C. Hein, R. Kautenburger, O. Clemens, and H. Hahn, *J. Eur. Ceram. Soc.* 38[5] (2018) 2318-2327.
162. P.B. Neto, L. Buss, F. Meierhofer, H.F. Meier, U. Fritsching, and D. Noriler, *Chem. Eng. Process.* 129 (2018) 17-27.
163. M. Ismael, A. Sharma, and N. Kumar, *Sustainable Mater. Technol.* 40 (2024) e00826.
164. S. Tada, K. Fujiwara, T. Yamamura, M. Nishijima, S. Uchida, and R. Kikuchi, *Chem. Eng. J.* 381 (2020) 122750.
165. L. Mädler, and S.E. Pratsinis, *J. Am. Ceram. Soc.* 85[7] (2002) 1713-1718.
166. K. Hembram, D. Sivaprakasam, T.N. Rao, and K. Wegner, *J. Nanopart. Res.* 15 (2013) 1461.
167. A.I.Y. Tok, F.Y.C. Boey, and X.L. Zhao, *J. Mater. Process. Technol.* 178[1-3] (2006) 270-273.
168. A.H. Phakatkar, M.T. Saray, M.G. Rasul, L.V. Sorokina, T.G. Ritter, T. Shokuhfar, and R. Shahbazian-Yassar, *Langmuir* 37[30] (2021) 9059-9068.
169. A. Sakar, R. Djenadic, N.J. Usharani, K.P. Sanghvi, V.S.K. Chakravadhanula, A.S. Gandhi, H. Hahn, and S.S. Bhattacharya, *J. Eur. Ceram. Soc.* 37[2] (2017) 747-754.
170. N.J. Löh, L. Simao, C.A. Faller, A. De Noni, and O.R.K. Montedo, *Ceram. Int.* 42[11] (2016) 12556-12572.
171. S. Biswas, D. Schwen, and V. Tomar, *J. Mater. Sci.* 53 (2018) 5799-5825.
172. S.H. Chen, Y.P.K. Xu, and Y. Jiao, *Modell. Simul. Mater. Sci. Eng.* 24[8] (2016) 085003.
173. J.M. Missiaen and J.M. Lebrun, *J. Am. Ceram. Soc.* 98[11] (2015) 3460-3468.
174. B. Wong and J.A. Pask, *J. Am. Ceram. Soc.* 62[3-4] (1979) 138-141.
175. Y.H. Huang, D.L. Jiang, J.X. Zhang, Z.M. Chen, Q.L. Lin, and Z.R. Huang, *J. Rare Earths* 32[5] (2014) 416-422.
176. Y.C. Wu and S.W. Chen, *Int. J. Hydrogen Energy* 42[44] (2017) 27284-27297.
177. F. Li, L. Zhou, J.X. Liu, Y.C. Liang, and G.J. Zhang, *J. Adv. Ceram.* 8 (2019) 576-582.
178. M.D. Qin, H. Vega, D.W. Zhang, S. Adapa, A.J. Wright, R.K. Chen, and J. Luo, *J. Adv. Ceram.* 11 (2022) 641-

- 655.
179. I.W. Chen, and X.H. Wang, *Nature* 404 (2000) 168-171.
  180. D. Yu, J. Yin, B.H. Zhang, X.J. Liu, M.J. Reece, W. Liu, and Z.R. Huang, *J. Eur. Ceram. Soc.* 41[6] (2021) 3823-3831.
  181. D. Yu, B.H. Zhang, J. Yin, Y.C. Wang, X.J. Liu, M.J. Reece, and Z.R. Huang, *J. Am. Ceram. Soc.* 105[1] (2022) 76-81.
  182. L. Gao, and H. Miyamoto, *J. Inorg. Mater.* 12 (1997) 129-133.
  183. Z.A. Munir, and M. Ohyanagi, *J. Mater. Sci.* 56 (2021) 1-15.
  184. Z.Y. Hu, Z.H. Zhang, X.W. Cheng, F.C. Wang, Y.F. Zhang, and S.L. Li, *Mater. Des.* 191 (2020) 108662.
  185. C.W. Park, J.H. Park, H.S. Kang, H.A. Lee, J.H. Lee, J.H. In, and K.N. Shim, *J. Ceram. Process. Res.* 19[5] (2018) 383-387.
  186. K.H. Kim, J.H. Chae, J.S. Park, D.K. Kim, K.B. Shim, and B.H. Lee, *J. Ceram. Process. Res.* 8[4] (2007) 238-242.
  187. Z.L. Liao, Q.L. He, W. Zhang, F. Zhang, W.M. Wang, and Z.Y. Fu, *Ceram. Int.* 50[13] (2024) 22443-22455.
  188. J. Guignard, M. Prakasam, and A. Largeteau, *Materials* 15[14] (2022) 4804.
  189. D. Zhang, L. Zhang, Z. Fu, J.K. Guo, and W.H. Tuan, *J. Mater. Sci.* 41 (2006) 293-295.
  190. A. Aliouat, G. Antou, N. Pradeilles, V. Rat, and A. Maître, *J. Alloys Compd.* 963 (2023) 171276.
  191. S.X. Song, Z. Wang, and G.P. Shi, *Ceram. Int.* 39[2] (2013) 1393-1393.
  192. M. Stuer, C.P. Carry, P. Bowen, and Z. Zhao, *J. Mater. Res.* 32 (2017) 3309-3318.
  193. S.T. Zhang, Z. Teng, L.Z. Wu, C. Chen, Y.Q. Tan, and X.S. Zhou, *Ceram. Int.* 50[3] (2024) 4573-4580.
  194. Y. Lu, H.B. Zhang, H.B. Yang, P.Y. Fan, C. Samart, N. Takesue, and H. Tan, *Crystals* 13[3] (2023) 445.
  195. Z. Teng, P. Wang, S.F. Zeng, W.L. Feng, C. Chen, P. Jia, Y.Q. Tan, and S.M. Peng, *Ceram. Int.* 50[4] (2024) 6892-6897.
  196. J. Gild, Y. Zhang, T. Harrington, S. Jiang, T. Hu, M.C. Quinn, M.M. Mellor, N. Zhou, K. Vecchio, and J. Luo, *Sci. Rep.* 6 (2016) 37946.
  197. Y. Zhang, W.M. Guo, Z.B. Jiang, Q.Q. Zhu, S.K. Sun, Y. You, K. Plucknett, and H.T. Lin, *Scr. Mater.* 164 (2019) 135-139.
  198. Y. Zhang, Z.B. Jiang, S.K. Sun, W.M. Guo, Q.S. Chen, J.X. Qiu, K. Plucknett, and H.T. Lin, *J. Eur. Ceram. Soc.* 39[13] (2019) 3920-3924.
  199. B.L. Ye, T.Q. Wen, K.H. Huang, C.Z. Wang, and Y.H. Chu, *J. Am. Ceram. Soc.* 102 (2019) 4344-4352.
  200. X.L. Yan, L. Constantin, Y.F. Lu, J.F. Silvain, M. Nastasi, and B. Cui, *J. Am. Ceram. Soc.* 101[10] (2018) 4486-4491.
  201. E. Castle, T. Csanádi, S. Grasso, J. Dusza, and M. Reece, *Sci. Rep.* 8 (2018) 8609.
  202. Y. Le Godec, and S. Le Floch, *Materials*, 16[3] (2023) 997.
  203. J.L. Wang, J. Li, Y. Li, L.L. Li, X.H. Su, Y.B. Hu, and X.Q. Xu, *Mater. Charact.* 209 (2024) 113771.
  204. S. Bhandari, T.P. Mishra, O. Guillon, D. Yadav, and M. Bram, *Scr. Mater.* 211 (2022) 114508.
  205. R. Mundra, T.P. Mishra, M. Bram, O. Guillon, and D. Yadav, *Int. J. Appl. Ceram. Technol.* 20[4] (2023) 2271-2280.
  206. A.F. Manchón-Gordón, A. Perejón, E. Gil-González, M. Kowalczyk, P.E. Sánchez-Jiménez, and L.A. Maqueda, *Materials* 16[1] (2023) 189.
  207. L. Niu, X.T. Han, Y. Zhou, H.T. Wang, X.R. Zhang, and J.H. Li, *Ceram. Int.* 50[9] (2024) 16684-16688.
  208. M. Biesuz and V.M. Sglavo, *J. Eur. Ceram. Soc.* 39[2-3] (2019) 115-143.
  209. J.L. Liu, D.A.G. Liu, K. Ren, and Y.G. Wang, *J. Inorg. Mater.* 37[5] (2022) 473-480.
  210. J.B. Xia, W. Ren, H. Sun, and B. Zhang, *Ceram. Int.* 50[9] (2024) 16111-16117.
  211. J.M. He, G.L. Zhao, T.W. Liu, and C. Xu, *J. Ceram.* 45[1] (2024) 32-45.
  212. A. Kumar, G. Sharma, A. Aftab, and I. Ahmad, *J. Eur. Ceram. Soc.* 40[8] (2020) 3358-3362.
  213. D.G. Liu, X.Y. Peng, J.L. Liu, L.Y. Chen, Y. Yang, and L.N. An, *J. Eur. Ceram. Soc.* 40[6] (2020) 2504-2508.
  214. W.G. Li, L.Y. Chen, D.G. Liu, J.L. Liu, and L.N. An, *Mater. Lett.* 304 (2021) 130679.
  215. B.S. Ma, Y. Zhu, K.W. Wang, Z.Z. Sun, K. Ren, and Y.G. Wang, *J. Am. Ceram. Soc.* 105[6] (2022) 3765-3773.
  216. K.W. Wang, B.S. Ma, T. Li, C.X. Xie, Z.Z. Sun, D.G. Liu, J.L. Liu, and L.N. An, *Ceram. Int.* 46[11] (2020) 18358-18361.
  217. G.L. Zhao, S.K. Cai, Y. Zhang, H. Gu, and C. Xu, *J. Eur. Ceram. Soc.* 43[6] (2023) 2593-2600.
  218. H.R. Mao, R.F. Guo, Y. Cao, S.B. Jin, X.M. Qiu, and P. Shen, *J. Eur. Ceram. Soc.* 41[4] (2021) 2855-2860.
  219. Z.K. Zhao, *Ceram. Int.* 47[4] (2021) 4389-4397.
  220. Y. Han, S. Li, T.B. Zhu, Z.P. Xie, *J. Am. Ceram. Soc.* 100[7] (2017) 2774-2780.
  221. Z.P. Xie, S. Li, and L.N. An, *J. Am. Ceram. Soc.* 97[4] (2014) 1012-1015.
  222. S. Li and Z.P. Xie, *J. Inorg. Mater.* 31[2] (2016) 207-212.
  223. M.L. Li, X.T. Zhao, G. Shao, H.L. Wang, J.P. Zhu, W. Liu, B.B. Fan, H.L. Xu, H.X. Lu, Y.C. Zhou, and R. Zhang, *Ceram. Int.* 47[6] (2021) 8707-8710.
  224. Y.C. Li, F. Xu, X.F. Hu, Y.B. Luan, Z.J. Han, and Z.Y. Wang, *Ceram. Int.* 41[10] (2015) 14554-14560.
  225. S.V. Egorov, A.G. Eremeev, V.V. Kholoptsev, I.V. Plotnikov, K.I. Rybakov, A.A. Sorokin, S.S. Balabanov, and E. Ye. Rostokina, *Ceram. Int.* 49[14] (2023) 24222-24228.
  226. R.H. Wang, J. Yang, D.N. Zou, P. Hu, and W.C. Xiang, *Mater. Rep.* 35[23] (2021) 23153-23161+23170.
  227. J.Y. Ma, *J. Phys. Chem. A* 120[41] (2016) 7989-7997.
  228. M. Oghbaei and O. Mirzaee, *J. Alloys Compd.* 494[1-2] (2010) 175-189.
  229. J. Liu, B.L. Liang, J.J. Zhang, and Y.L. Ai, *Mater. Rep.* 36[3] (2022) 136-145.
  230. J. Sun, W.L. Wang, and Q.Y. Yue, *Materials* 9[4] (2016) 231.
  231. P.T. Xie, Z.C. Shi, M. Feng, K. Sun, Y. Liu, K.L. Yan, C.Z. Liu, T.A.A. Moussa, M.N. Huang, S.W. Meng, G.M. Liang, H. Hou, R.H. Fan, and Z.H. Guo, *Adv. Compos. Hybrid Mater.* 5 (2022) 679-695.
  232. X. Zou, P.A. Chen, G.P. Xu, X.C. Li, Y.L. Zhu, and B.Q. Zhu, *China's Refract.* 32[4] (2023) 22-27.
  233. Y.C. Li, F. Xu, X.F. Hu, Y.B. Luan, Z.J. Han, and Z.Y. Wang, *J. Mater. Res.* 30 (2015) 3663-3670.
  234. N.N. Wang, W.H. Zou, X.Y. Li, Y.Q. Liang, and P. Wang, *RSC Adv.* 12[27] (2022) 17158-17181.
  235. W.L. Wang, B. Wang, J. Sun, Y.P. Mao, X.Q. Zhao, and Z.L. Song, *RSC Adv.* 6[58] (2016) 52974-52981.
  236. H. Jin, J. Lee, L. Zhuang, S. Yeom, H.S. Shin, and Y.J. Kim, *J. Build. Eng.* 88 (2024) 109193.

237. B.Z. Song, W.Z. Dong, L. Guan, Y.Z. Lou, Y.J. Zhu, J.X. Zhang, L. Fan, X.Q. Guo, G. Shao, and R. Zhang, *Ceram. Int.* 50[13] (2024) 22232-22242.
238. C.W. Wang, W.W. Ping, Q. Bai, H.C. Cui, R. Hensleigh, R.L. Wang, A.H. Brozena, Z.P. Xu, J.Q. Dai, Y. Pei, C.L. Zheng, G. Pastel, J.L. Gao, X.Z. Wang, H. Wang, J.C. Zhao, B. Yang, X.Y. Zheng, J. Luo, Y.F. Mo, B. Dunn, and L.B. Hu, *Science* 368[6490] (2020) 521-526.
239. Q.Q. Li, H.L. Du, X. Zhao, F. Zhao, Y.C. Zhang, X.J. Hu, and X. Du, *Ceram. Int.* 50[11] (2024) 18907-18914.
240. M. Kermani, C.F. Hu, and S. Grasso, *Ceram. Int.* 49[3] (2023) 4017-4029.
241. L. Spiridigliozzi, G. Dell'Agli, S. Esposito, P. Rivolo, S. Grasso, V.M. Sglavo, and M. Biesuz, *Scr. Mater.* 214 (2022) 114655.
242. F.X. Ye, F.W. Meng, T.Y. Luo, and H. Qi, *Ceram. Int.* 48[23] (2022) 35649-35654.
243. F.X. Ye, F.W. Meng, T.Y. Luo, and H. Qi, *J. Eur. Ceram. Soc.* 42[11] (2022) 4686-4691.
244. R.F. Guo, H.R. Mao, Z.T. Zhao, and P. Shen, *Scr. Mater.* 193 (2021) 103-107.
245. H. Xie, M.D. Qin, M. Hong, J.C. Rao, M. Guo, J. Luo, and L.B. Hu, *Sci. Adv.* 8[27] (2022) eabn8241.